Revisiting the Global Patterns of Seasonal Cycle in Sea Surface Salinity

Lisan Yu[1], Frederick M. Bingham[2], Tony Lee[3], Emmanuel P. Dinnat[4], Severine Fournier[3], Oleg Melnichenko[5], Wenqing Tang[3], and Simon H. Yueh[3]

[1] Woods Hole Oceanographic Institution, Woods Hole, MA 02543, USA

[2] Center for Marine Science, University of North Carolina Wilmington, Wilmington, NC 28403, USA

[3] Jet Propulsion Laboratory, California Institute of Technology, Pasadena, CA 91109, USA

[4] NASA Goddard Space Flight Center, Greenbelt, MD 20785, USA; Chapman University, CEESMO, Orange, CA 92866, USA.

[5] International Pacific Research Center, University of Hawaii, Honolulu, HI 96822, USA

February 2021

Main points

1. Harmonic analysis was applied to four 0.25° satellite products (SMAP and SMOS) and two 1° in situ products (Argo and EN4) between 2016-2018.
2. The annual and semiannual harmonic patterns estimated from satellite products have a good agreement with the 0.25° World Ocean Atlas 2018.
3. In situ products underrepresent small-scale SSS variability when data record is short, affecting the variance explained by annual harmonic.

Abstract

Argo profiling floats and L-band passive microwave remote sensing have significantly improved the global sampling of sea surface salinity (SSS) in the past 15 years, allowing the study of the range of SSS seasonal variability using concurrent satellite and in situ platforms. Here harmonic analysis was applied to four 0.25° satellite products and two 1° in situ products between 2016 and 2018 to determine seasonal harmonic patterns. The 0.25° World Ocean Atlas (WOA) version 2018 was referenced to help assess the harmonic patterns from a long-term perspective based on the three-year period. The results show that annual harmonic is the most characteristic signal of the seasonal cycle, and semiannual harmonic is important in regions influenced by monsoon and major rivers. The percentage of the observed variance that can be explained by harmonic modes varies with products, with values ranging between 50 and 72 % for annual harmonic and between 15 and 19% for semiannual harmonic. The large spread in the explained variance by the annual harmonic reflects the large disparity in nonseasonal variance (or noise) in the different products. Satellite products are capable of capturing sharp SSS features on meso- and frontal scales and the patterns agree well with the WOA 2018. These products are, however, subject to the impacts of radiometric noises and are algorithm dependent. The coarser-resolution in situ products may underrepresent the full range of high-frequency small scale SSS variability when data record is short, which may have enlarged the explained SSS variance by the annual harmonic.

Plain Language Summary

The seasonal cycle is the dominant signal of sea surface salinity (SSS) variability. Although often removed in studies concerning climate variability, the seasonal cycle of SSS is of great interest in its own right. SSS is a fundamental state variable and an indicator of the changes in the global water cycle. SSS together with sea surface temperature (SST) determines the near-surface buoyancy and density stratification, influencing the water mass formation, ocean circulation, marine ecosystem, and biogeochemistry. Previous studies of seasonal SSS were based on observations that were sparsely distributed in some parts of the ocean. SSS records with seasonal resolution have become more readily available with the advent of the global Argo array of profiling floats since 2003 and the L-band passive microwave remote sensing since 2010. This study analyzed a suite of SSS data records from recent satellite and in situ platforms, aiming to provide a characterization of the seasonal range of SSS in both the tropical low-SSS regime associated with the Intertropical Convergence Zone (ITCZ) and the subtropical high-SSS regime under the influence of high evaporation. The findings of the study will be useful for understanding potential advantages and limitations of the SSS observing system.

1. Introduction

The advent of L-band passive microwave remote sensing in the last decade (2010 to present) has allowed for the first time the retrieval of global high-resolution sea surface salinity (SSS) from space (Reul et al. 2014; Vinogradova et al. 2019). These new SSS datasets have opened the modern era of salinity science, leading to new insights into the role of salinity in ocean circulation, water mass formation, the water cycle, and climate variability and change (Reul et al. 2020). Like many typical time series, the most characteristic signal of satellite SSS is the seasonal cycle, a pattern that is repetitive from year to year and has variability generally greater than intraseasonal, interannual, and longer-timescale variability (Bingham & Lee, 2017; Dinnat et al., 2019). To facilitate the detection of climate-induced fluctuations that have smaller magnitudes, the seasonal cycle is often removed in studies concerning climate variability. However, the seasonal cycle of SSS is of great interest in its own right. SSS is a fundamental ocean state variable which, together with sea surface temperature (SST), determines the buoyancy and density stratification of the near-surface ocean. It has been shown that changes to the seasonal salinity patterns alter the timing, magnitude, and spatial distribution of water-column stratification (Maes & O'Kane 2014; Jensen et al. 2016), which in turn influences the preconditions for water mass formation (Yu et al. 2018; Piracha et al. 2019) and open-ocean deep convection (Gelderloos et al. 2012; Cherniavskaia et al. 2018), and modifies the production and seasonal cycle of ecosystem dynamics (Greene 2013). Systematic and accurate quantification and characterization of seasonal variations of SSS are highly needed. This is especially necessary for satellite SSS observations because they are new and need to be fully evaluated and understood (Bingham et al. 2021).

There are generally two approaches to obtain the seasonal cycle of a multi-year time series. One is to average values for the same month for different years over the available period. The other is to subject the time series to harmonic analysis and estimate the amplitudes and phases of the annual and semiannual cycles. Levitus (1986) and Boyer and Levitus (2002; hereafter BL2002) were among the first works that provided a comprehensive view of the annual cycle of global SSS using the World Ocean Atlas 1998 (WOA98) fields of climatological monthly mean salinity (Boyer & Levitus 1994). In particular, BL2002 computed the annual and semi-annual harmonics from Fourier analysis and showed that most of the world ocean has an annual cycle of SSS less than 0.3 on the practical salinity scale (pss). Areas with the annual cycle larger than 0.3 pss include the tropical Pacific and Atlantic under the Intertropical Convergence Zone (ITCZ) and the South Pacific Convergence Zone (SPCZ), the Northern Indian Ocean that is impacted by the monsoons, and the northern North Atlantic that is subject to Arctic meltwater discharge. They also showed that the amplitude of the second harmonic is greater than 0.3 pss only in limited areas, mostly the outflow regions that are affected directly by major rivers including the Amazon (the western tropical Atlantic), Congo and Niger (the equatorial eastern Atlantic), Mississippi (the northern Gulf of Mexico), and Ganges/Brahmaputra (the Bay of Bengal).

The WOA98 climatology is an objectively analyzed gridded product derived from profile data archived in the World Ocean Database 1998 (WOD98; Boyer et al., 1998). Although the total number of SSS observations in the WOD98 exceeds 1.4 million over a 45-year span, the spatial and temporal data distribution is highly inhomogeneous. There is greater data coverage for the Northern Hemisphere than the Southern Hemisphere, a greater amount of data for summer months than for winter months, and more observations in the open oceans than in the coastal zones. Despite of these uncertainties, the work of BL2002 laid a solid foundation for further study of SSS seasonal variability that uses improved datasets and with enhanced regional foci. For instance, Rao and Sivakumar (2003) used the North Indian Ocean subset of the WOD98 and examined the dynamical contrast between the SSS seasonal distributions of the Arabian Sea (AS) and Bay of Bengal (BoB). Bingham et al. (2010) produced composite maps of near-surface salinity seasonal cycles in the Pacific by adding a large thermosalinograph and bucket salinity database collected by French researchers (Delcroix et al., 2005) and a significant number of new profiling-float data in the Pacific that were collected since the work of BL2002. They also applied harmonic analysis to individual data instead of monthly-gridded values. Chen et al. (2018) took the advantage of the 11-year (2004–2014) Argo monthly-mean fields (Roemmich & Gilson 2009) and conducted harmonic decomposition to obtain the three-dimensional structure of the global salinity seasonal climatology. The annual and semiannual periodicities can be found from the surface all the way down to the Argo sampling depth of ~ 2000 m. There are also a few applications to recent satellite SSS products in various selected regions (e.g., Reagan et al. 2014; Sena Martins et al. 2015; Köhler et al. 2015; Melnichenko et al. 2019; Yu 2020).

Wyrtki (1965) pointed out that the harmonic parameters provide a direct measure for the amplitudes of annual and semiannual cycles. These parameters are more straightforward in capturing the dominant harmonic patterns of seasonal variations than a set of monthly maps produced by the averaging approach. However, this approach is not suitable if the objective is to gain an understanding of the processes responsible for the seasonal variations in the time series. In this regard, one often uses the seasonal cycle produced by the averaging approach to compute the contribution of each physical process (e.g. surface fluxes, advection, and mixing) to the total budget of salt (for salinity) or heat (for temperature). Seasonal SSS dynamics based on the near-surface budget equations have been applied to almost all ocean basins, including but not limited to the tropical Pacific (Delcroix et al. 1996; and Alory et al. 2012), the tropical Indian Ocean (Rao & Sivakumar, 2003; Köhler et al. 2015), the tropical Atlantic (Foltz et al. 2008; Camara et al. 2015), the pan-tropical ocean (Hasson et al. 2013a; Yu 2015), the subtropical ocean (Johnson et al. 2016), the Southern Ocean (Dong et al. 2009; Ren et al. 2011), the global ocean (Yu 2011; Bingham et al. 2012; Vinogradova & Ponte 2013), and the plume at the mouth of the Mississippi River (Fournier et al. 2016). Some of the studies listed above included both the annual harmonic analysis and the mixed layer salt budget analysis (e.g. Rao & Sivakumar 2003; Bingham et al. 2012; Vinogradova & Ponte 2013; Köhler et al. 2015).

This study aims to examine the SSS seasonality using satellite SSS products derived from two L-band missions: the Soil Moisture and Ocean Salinity (SMOS) mission by the European Space Agency (ESA) that has been providing continuous SSS data record since a few weeks after its launch in November 2009 (Kerr et al. 2010; Reul et al. 2020), and the NASA's Soil Moisture Active Passive (SMAP) mission that has been operating since January 2015 (Entekhabi et al. 2010; Vinogradova et al. 2019). The L-band radiometers operate on the principle that the emissivity from the ocean surface is dependent on the dielectric constant of seawater and is a function of salinity, temperature, sea surface state, polarization, and incidence angle (Swift & McIntosh 1983; Lagerloef et al. 1995; Yueh et al. 2001). However, the radiometric sensitivity to SSS is highly dependent on SST, decreasing from 0.7K per pss change for SST of 30°C to 0.25 K per pss change for SST of 0°C. In addition, the SSS retrievals are affected by geophysical signals (e.g. SST, sea surface state such as roughness, foam, and whitecaps) and external perturbations including extraterrestrial contributions (e.g. galactic/cosmic background radiation and sun glint), antenna-radiation emission, Faraday rotation in Earth's ionosphere, atmospheric attenuation, and Radio Frequency Interference (RFI) (Boutin et al. 2004; Le Vine et al. 2005; Reul et al. 2007; Oliva et al. 2012; Dinnat et al. 2019). The latter results from the unauthorized use of the protected L-band or out-of-band contamination in some coastal areas or a leakage of other radar signals into L-band. SMOS and SMAP SSS products have been validated extensively with in situ salinity measurements, showing that the accuracy of 0.2 pss can be met between 40°S and 40°N (Boutin et al. 2018).

The focus of this study is the ocean between 50°S and 50°N, where the open-water surface temperature is mostly between 5–30°C throughout the year and SSS retrievals are better validated. One main objective is to produce a global pattern of SSS seasonal cycle by using the gridded products derived from recent satellite and in situ platforms. Four 0.25° satellite SSS products are analyzed, with two from SMAP (Fore et al. 2020; Meissner et al. 2019) and two from SMOS (Boutin et al. 2019; SMOS-BEC Team, 2019). These products are developed independently by different groups using different retrieval algorithms. To compare with their in-situ counterpart, two in situ gridded salinity products are included in the analysis: the 1° salinity product gridded by the Scripps Institution of Oceanography from Argo profile floats (Roemmich & Gilson 2009; hereafter referred to as the Argo product) and the version 4 of the Met office Hadley Centre "EN" series of monthly 1° objective analysis of salinity (Good et al. 2013; hereafter referred to as the EN4 product).

The six contemporary SSS products have a higher temporal and spatial resolution and greater sampling homogeneity than the WOD98 used in BL2002. Reul et al. (2020) pointed out that satellites provide quasi-instantaneous swath measurements that represent averages over radiometer footprints with typical scales of 40–150 km. Since the early 2000s, the Argo array of profiling floats covers the global open ocean with average spacing of about 300 km (i.e. a nominal spatial sampling resolution of 3° × 3°; Riser et al. 2016), which dramatically increases the global density of near-surface salinity measurements (see Figure 11 in Reul et al. (2020)).

The overlapping time between the six chosen products is relatively short, about three years (2016-2018) at the time this work was conducted. The three-year time period raises a question as to whether it is sufficient to depict the mean features that are defined by a longer time period. However, BL2002 is not an ideal reference for addressing this question because the WOD98 suffered from sampling bias and underrepresented a large part of the ocean. The salinity climatology in the latest World Ocean Atlas version 2018 (hereafter WOA) presents a better long-term reference. WOA has a version gridded on 0.25°×0.25° spatial resolution (Zweng et al. 2018) as a result of the increased number of observations since the WOD98. This study will use the WOA as a reference in assessing the climatological aspect of the recent SSS products.

The paper is organized as follows. A description of the datasets and the method is provided in Section 2. Mean and seasonal variability of SSS are evaluated in Section 3. The results obtained from the harmonic analysis are presented in Section 4. Summary and discussion are given in Section 5.

2. Data and methods

2.1 Data sets

Major characteristics of the six SSS products and the WOA are listed in Table 1. A brief description of each dataset is provided below.

2.1.1 Satellite SSS products

Two SMAP products used in the study are the SMAP Level 3 version 4.3 by the Jet Propulsion Laboratory (JPL) (hereafter referred to as SMAP JPL) (Fore et al. 2020), and the SMAP Level 3 Remote Sensing Systems (RSS) product (hereafter referred to as SMAP RSS) recently released version 4.0 (Meissner et al. 2019). The SMAP JPL product features a 60-km spatial resolution and include an 8-day running mean dataset and a monthly average dataset, all on a 0.25°×0.25° grid (Fore et al. 2020). The SMAP RSS product is also available with 8-day running means and monthly averages; these products are resampled on a 0.25°×0.25° grid from a 70-km spatial feature resolution using a Backus-Gilbert type optimum interpolation (OI) to reduce random noise (Meissner et al., 2018).

The two SMOS products are the SMOS SSS Level 3 maps produced by the Laboratoire d'Océanographie et du Climat (LOCEAN) and Centre Aval de Traitement des Données SMOS (CATDS) (Boutin et al. 2019; hereafter referred to as SMOS LOCEAN), and the Level 3 version 2 SMOS SSS global product from the Barcelona Expert Center (BEC) (SMOS-BEC Team, 2019; hereafter referred to as SMOS BEC). SMOS LOCEAN applied a de-biasing technique that improves ice filtering and SSS at high latitudes (Boutin et al. 2019). The 9-day running mean maps have 25-km × 25-km spatial resolution. SMOS BEC data are generated using a debiased non-Bayesian approach (Olmedo et al. 2017), which corrects systematic biases caused by land masses and RFI and improves the data gaps due to the non-convergence of the retrieval algorithm. The 9-day running objectively analyzed Level 3 maps are provided daily at 0.25°× 0.25° spatial resolution. In this study, the two SMOS products were monthly averaged and mapped on the same 0.25°× 0.25°grids as the two SMAP products. Three full overlapping years (2016-2018) were analyzed.

2.1.2 In situ gridded SSS products

The two in situ gridded SSS products are the Argo (Roemmich and Gilson 2009) and EN4 (Good et al. 2013) monthly objective analyses. The Argo product is constructed from more than 3000 autonomous profiling floats over the global ocean. It is obtained by first estimating the time-mean field using a weighted local regression fit to several years of Argo data and then applying optimal interpolation on the mean-subtracted monthly residuals to obtain the interpolated anomaly fields on 1°×1° grids. Salinity data in the topmost layer at a depth of 2.5 m is used as SSS in this study. The EN4 1°×1° gridded monthly data products are compiled from quality-controlled temperature and salinity profiles that are sourced from the Global Temperature and Salinity Profile Programme (GTSPP), World Ocean Database 2009 (WOD09), and Argo. Because of the use of Argo profiling float data, the EN4 product is not independent of the Argo product. The use of non-Argo data in EN4 is essential in regions where Argo floats are limited or not available, such as in shallow coastal waters, marginal seas, and sea-ice marginal zones (Reagan et al. 2014). The topmost grid level of EN4 is at a depth of 5.25 m below the surface, and is used as SSS to compare with satellite SSS products.

2.1.3 WOA

The WOA has both 1° and 0.25° gridded climatologies that were constructed from the mean average of six “decadal” climatologies for the following time periods: 1955–1964, 1965–1974, 1975–1984, 1985–1994, 1995–2004, and 2005–2017 (Zweng et al. 2018). The substantial addition of historical salinity data since the publication of WOD98 has increased data density over the global ocean, allowing the salinity climatology to be gridded to the 0.25°×0.25° resolution used in this study. Zweng et al. (2018) cautioned, however, that even with these additional data, the WOA may still be hampered by a lack of data in some areas. The topmost grid level of the WOA is at the ocean surface (depth = 0 m).

2.1.4 Satellite versus in situ SSS

It should be noted that the Argo and EN4 SSS are considered to be a bulk SSS, representative of the salinity at about 5-m depth. Satellite SSS is a skin SSS, determined by the depth at which the incoming power density is reduced by one order of magnitude (Boutin et al. 2016). For L-band microwave radiometers, the skin layer is about 1 cm at SST of 20°C (Swift 1980). Skin SSS can be different from bulk SSS if there are vertical salinity gradients between the two measurement depths (Yu 2010; Drucker and Riser, 2014; Henocq et al., 2010; Song et al. 2015). This situation usually occurs in calm wind and high precipitation conditions, or within river plumes (Boutin et al. 2016). However, in situ simultaneous measurements of skin (very close to the surface) and bulk salinities are lacking, which hampers our ability to characterize the conditions that generate the vertical salinity stratification at the near surface. It is yet to be known whether, when, and how the skin-bulk SSS differences could be a source of bias affecting the interpretation of the findings of this study.

Another major difference between satellite and in situ SSS is the sampling frequency in both space and time. Reul et al. (2020) pointed out that satellites provide quasi-instantaneous swath measurements that represent averages over radiometer footprints with typical scales of 40–150 km. Space-time composites of swath satellite SSS are the basis of the 8-day mean or monthly mean global SSS products. On the other hand, in situ platforms (including Argo floats) provide pointwise samples. To produce gridded products, the pointwise measurements are optimally interpolated using a pre-specified radius of influence, or decorrelation scale, that defines the distance to which the influence of the point measurement is significant (e.g. Good et al. 2013; Zweng et al. 2018). Data density is of paramount importance in determining the spatiotemporal representation of the resultant gridded products. Since the early 2000s, the global Argo array of profiling floats have dramatically increased the global density of near-surface salinity measurements (Roemmich & Gilson 2009). The Argo floats surface every ~ 10 days and the typical distance between floats is on the order of 300km (i.e. a nominal spatial sampling resolution of 3° × 3°; Riser et al. 2016). The target resolution is much coarser than the SMAP and SMOS sampling resolution (40–50 km) (see Figure 7 in Reul et al. 2020). Reul et al. (2020) showed the many differences between satellite and Argo SSS products in regions of strong SSS gradients generated by rain bands (e.g. Yu 2015), river plumes (e.g. Fournier et al. 2017a), or strong eddy currents (e.g. Abe et al. 2019), where Argo observations are either unavailable due to the close proximity to the coast or unable to resolve meso- and frontal-scale variability due to the lack of sufficient resolution.

The focal domain of this study is the ocean basin between 50°S and 50°N where SST is sufficient high and SSS products are better validated. For the analysis of satellite SSS products at higher latitudes (poleward of 50°N/S), readers are referred to recent studies by Köhler et al. (2015), Garcia-Eidell et al. (2017, 2019), Fournier et al. (2019), Tang et al. (2018, 2019), and Yu (2020).

2.2 Harmonic analysis

A least-squares fit of the annual and semi-annual harmonics to the time series at each grid point was performed based on the following equation (Wyrtki 1965; Wilks 1995):

$$S(t) = S_0 + A_1 \cos(\omega_1 t + \varphi_1) + A_2 \cos(\omega_2 t + \varphi_2) \quad (1)$$

where S is the monthly-mean SSS at time t expressed in months (total 36 months in this study), S_0 is the three-year mean salinity, ω_1 and ω_2 are the annual and semiannual frequencies expressed as $\omega_1 = 2\pi/12$ months, $\omega_2 = 2\pi/6$ months, and A_1, A_2, φ_1, and φ_2 are the amplitudes and phases of the annual and semiannual harmonics, respectively. At each grid point, the amplitudes (A_1 and A_2) and phases (φ_1 and φ_2) were computed from the regression procedure using the three-year time series. Harmonic analysis was also applied to the 12-month WOA climatology to provide a climatological reference.

Two statistical measures are often used to evaluate how much the observed annual variance can be explained by the first and second harmonics respectively. The first measure is the R^2 value, calculated from the following formula

$$R^2 = \left(1 - \frac{\text{variance(data} - \text{harmonic mode)}}{\text{variance (data)}}\right) \times 100 \qquad (2)$$

The R^2 values in this study are reported as percentages from 0% to 100%. A high R^2 value indicates a higher amount of variability being explained by the respective harmonic mode. The second measure is the F-statistic that tests whether the data product and the respective harmonic mode has the same variance. Following Bingham et al. (2021), the F-statistic was calculated from R^2 using the equation

$$\mathrm{F} = \frac{R^2}{1 - R^2} \cdot \frac{N - m - 1}{m} \qquad (3)$$

where N is the number of observations and m is the number of independent harmonic modes, which is 2 in our case of examining the annual and semiannual harmonics. The F values were calculated assuming all data points were independent observations, and significance was defined as the F values being greater than 0.95.

3. Mean and seasonal variability of SSS

3.1 The three-year mean SSS fields

The three-year (2016–2018) mean SSS fields constructed from the six products are shown (Figure 1). Fundamental features of the mean SSS distribution include the contrast between the saltier Atlantic Ocean and the fresher Pacific and Indian Oceans at all latitudes, SSS minima (hereafter Smin) in regions of the ITCZ and SPCZ and higher latitudes, and SSS maxima (hereafter Smax) in the subtropical ocean. A well-defined Smax center exists in all subtropical regimes of the Pacific, Atlantic, and the Indian Oceans.

The tropical Smin and the subtropical Smax reflect the time-mean interactions between the evaporation-minus-precipitation (E–P) flux, ocean circulation, and mixing processes (e.g. Dessier & Donguy 1993; Delcroix et al. 1996; Donguy & Meyers 1996; Talley 2002; Gordon et al. 2015; Melzer & Subrahmanyam 2015; Hasson et al. 2013b; and references therein). Marked low-salinity surface waters are also noted in the coastal areas near major rivers, including the northern Bay of Bengal, the eastern equatorial Pacific and Atlantic, the western equatorial Atlantic, the East China Sea, and the northwestern Atlantic shelf region. This localized freshening is dictated by the hydrological forcing through local rainfall and river discharges (Gierach et al. 2013; Grodsky et al. 2014; Chao et al. 2015; Fournier et al. 2017a&b; da Silva & Castelao 2018). In general, plume features are underestimated in in situ products (Fournier & Lee 2021).

3.2 The three-year mean versus the long-term mean climatology

The WOA at 0.25° × 0.25° resolution is taken as a reference to assess how the three-year mean pattern deviates from the long-term mean climatology. The 1°× 1° Argo and EN4 fields were interpolated onto 0.25°× 0.25° grids so that all six means are gridded in the same way and then the WOA was subtracted from each product (Figure 2). The most coherent feature among the six difference anomaly patterns is the basin-scale negative difference anomalies, most evident in the Pacific Ocean north of 20°S. These negative anomalies, with a magnitude mostly between –0.2 and –0.1 pss in all products except for SMOS BEC, indicate that the recent SSS products are mostly fresher than the WOA climatology of 60+ years.

In general, SMOS BEC has the smallest difference anomalies and the best overall agreement with WOA. The five other SSS products show also considerable deviation from WOA in other parts of the ocean. SMAP JPL (Figure 2a) is saltier than WOA (positive anomalies) in the equatorial Pacific and Atlantic cold tongue regions and the Arabian Sea, but fresher (negative anomalies) in most of the Southern Hemisphere. SMAP RSS (Figure 2b) has negative anomalies almost everywhere except for the North Atlantic and the latitude band between 40 – 20°S in the South Pacific. Large positive anomalies (> 0.2 pss) are present in the coastal regions adjacent to the South American continent and the neighborhood of the Caribbean Seas and Gulf of Mexico. SMOS LOCEAN (Figure 2c) has negative anomalies in the Pacific and also in the South Indian and South Atlantic, but positive anomalies (> 0.2 pss) in the Arabian Sea and the Northwest Atlantic. The two in situ gridded products, EN4 and Argo, have a similar difference pattern (Figures 2e-f). Both show the dominance of negative anomalies in the Pacific and the eastern tropical Indian Ocean and the dominance of positive anomalies in the Northeast Pacific and the North Atlantic Ocean. The Argo product has no observations in coastal regions.

3.3 Mean and mean difference between the six products

The WOA-based evaluation reveals a similar large-scale anomaly pattern among the six mean SSS fields, suggesting a broad consistency between the six SSS means. To see this more clearly, standard deviations (STDs) were computed (Figure 3b) to quantify the spread between the six mean fields (Figure 3a). STDs are small in the open ocean away from the coast and equatorial regions, generally less than 0.05 pss. However, the six STD patterns show considerable differences between products (STD> 0.2 pss) in the periphery and coastal areas, the marginal seas, the ITCZ and SPCZ regions, and some higher latitude areas (poleward of 40°N/S).

Nine boxes surrounding the tropical Smin and subtropical Smax are drawn on Figure 3. These selected areas are the key sites for the characterization of seasonal variability of SSS extrema in the following sections of this paper. Locations, abbreviated names, and the product ensemble SSS mean and STD (spread) within the nine boxes are listed in Table 2. There are three Smin boxes (1-3) in the tropical low-SSS regime, one in each basin, located primarily in the open ocean away from the direct influence of major rivers. There are six subtropical Smax boxes (4-9) around the subtropical high-SSS zones in both the Northern and Southern Hemispheres.

The Smax boxes (4-9) are generally located in regions of low STD values (0.02 – 0.03 pss) between products, except for the Arabian Sea (Box 6) where the STD (spread) between the products is large, about 0.13 pss (Table 2). For the three Smin boxes, the STD is about 0.03 pss in the tropical Atlantic (Box 2) but is 2-3 times larger in the eastern tropical Pacific (Box 1) and the Bay of Bengal (Box 3).

The ensemble mean SSS map is shown in Figure 3a with the nine boxes superimposed. The mean value averaged over each of the nine boxes (Column 5 in Table 2) is listed. For boxes

4-9, the contour that represents the SSS mean value of the box is drawn for each product using different colors.

3.4 Seasonal variability of SSS

The STD of the monthly-mean SSS values is used as a measure of SSS seasonal variability (Figure 4). Argo shows that large STDs (>0.4 pss) dominates the following areas: the pan-tropical low salinity zone under the ITCZ and SPCZ, the near coastal areas affected by the Amazon plume in the western tropical Atlantic (Grodsky et al. 2014; Fournier et al. 2017b) and the Congo and Niger rivers in the eastern equatorial Atlantic (Reul et al. 2014; Chao et al. 2015), the northwestern Atlantic shelf region particularly south of the St. George's and Newfoundland banks (Grodsky et al. 2017), the northern Gulf of Mexico bordering the Mississippi (da Silva and Castelao, 2018), the vicinity of the western South Atlantic near 35°S, 55°W under the influence of the Rio de la Plata (Piola et al. 2005), the Bay of Bengal impacted by monsoon and the Ganges/Brahmaputra river (Momin et al. 2015; Fournier et al.2017a), and the southeastern Arabian Sea centered at 8°N, 75°E, known as the Laccadive Sea region (also called the Lakshadweep Sea) (Bruce et al. 1994; Schott & McCreary 2001). All of these high STD regions are in direct response to the freshwater sources from rainfall and/or river discharge, except for the high STD in the Laccadive Sea of the Arabian Sea. In the latter, the source of the pronounced seasonal variability of SSS is the incursion of the Bay of Bengal water from November to February (Sasamal 1990; Shenoi et al., 1999; Jensen 2001). During that period, the Northeast Monsoon generates the East Indian Coastal Current (EICC) that flows equatorward along the Indian and Sri Lankan coast and brings low-salinity water from the Bay of Bengal to the southeast Arabian Sea (D'Addezio et al., 2015), freshening the sea-surface by more than 1 pss compared to October (Rao & Sikakumar 2003).

The STD patterns show that the SMOS BEC product is significantly different from the other products. The three satellite products, SMAP JPL, SMAP RSS, and SMOS LOCEAN (Figures 4a-c) have a broad agreement with Argo in the tropical regions but show large deviations in two other areas. One is the North Pacific north of 40°N where SMAP JPL, SMAP RSS, and SMOS LOCEAN have abnormally high STDs (>0.4 pss). The other area is the western Arabian Sea off the coast of Oman where the STDs are high (>0.4pss) in the two SMOS products, but much smaller in SMAP and in situ products. Zonal bands of high STDs are also seen in SMAP JPL at high southern latitudes (poleward of 40°S). Among the four satellite products, SMOS BEC has the weakest STDs, particularly in the tropical Pacific under the ITCZ and SPCZ.

The EN4 STD pattern is similar to that of Argo over the open ocean, but has enhanced STD values in the marginal seas and coastal areas. The differences are due primarily to the differences in data coverage. Argo floats do not sample shallow seas and coastal areas, whereas the EN4 product includes in situ measurements from all available platforms and refers to long-term climatology as background information in the presence of data gaps (Good et al. 2003).

One marked difference between satellite and in situ SSS products is the mean level of STD in the open ocean away from the tropical rain bands and the coastal zones. In these seasonally quiescent regions, the STDs in Argo and EN4 are small, at 0.1 pss or less. However, satellite products have considerably higher STDs, with magnitude generally above 0.1 pss. The differences could be caused by two reasons: either satellite products contain a higher level of random noise, or in situ products underestimate seasonal variability in the open ocean.

4. Patterns of Harmonic Modes

4.1 Annual harmonic of SSS

Amplitudes of the estimated first harmonic (A_1 in Eq. (1)) in the six SSS products (Figure 5) show that the regions of large STDs (>0.3 pss; Figure 4) are also regions of pronounced annual cycle, with SSS amplitudes exceeding 0.3 pss. As mentioned in the previous section, these areas are predominantly influenced by the freshwater sourced from either rainfall or river discharge, demonstrating the intimate connection of the regional SSS to the ocean and terrestrial water cycle. The six products agree well with each other on the annual harmonic pattern. It is worth noting, however, that SMOS BEC has the weakest annual amplitude over the global ocean, showing almost no annual variation in the extratropical open ocean. SMAP JPL has larger annual amplitudes than the other products in the sub-polar North Pacific, poleward of 40°N, and also in the Southern Ocean near 40°S.

The phase of the estimated annual cycle (φ_1 in Eq. (1)) represents the occurrence time (month of the year) of the maximum SSS (i.e, the saltiest surface water). Patterns of the annual phase (Figure 6) suggest that the six products are consistent in describing the progression of the maximum amplitude of the SSS annual cycle in the tropical ocean. For instance, SSS at the 10°N latitude band in the tropical Pacific reaches the annual maximum in April-May when the ITCZ is located near the equator, whereas SSS near the equator has the annual maximum in July-August where the ITCZ moves farthest north near 10°N. Similar annual phase progression is also shown in the tropical Atlantic and Indian Oceans, with a noted exception of SMOS BEC which has a phase shift in the North Indian Ocean.

Outside of the tropical oceans, the satellite products deviate from one to another in two zonal bands. One is the Southern Hemisphere between 50–20°S, where SMOS BEC is markedly different from the other products, showing that the annual high SSS values occur predominantly in February, compared to November and April for the other products. The second location is the Northern Hemisphere between 20–40°N with one center located in the northwestern Pacific off the coast of Japan (120°E – 180) and the other center located in the northwestern Atlantic off the coast of the United State and Canada. In these regions, the phase in SMOS BEC and SMOS LOCEAN is shifted by about 6 months. The SMAP JPL and SMAP RSS products are similarly out of phase with in situ products, showing a phase shift of about 3 months in the northwestern Pacific. Apparently, satellite products have a biased seasonal SSS phasing in this zonal band.

One possible factor contributing to such seasonal biases is the effect of RFI. The percentages of SMAP land samples suspected to be influenced by RFI are highly concentrated in the regions such as near Japan and northeastern China as well as off the coast of Europe (e.g., Piepmeier et al 2014). Even if some SMAP measurements over the ocean that are obviously affected by RFI are excluded, low-level RFI can still affect satellite SSS retrievals. SMOS is also significantly affected by RFI and land contamination in these regions, and exhibits very large positive biases in radiometric observations (resulting in fresh biases in retrieved salinity) extending to 160°E and beyond east of Japan (Martín-Neira et al., 2016). Some mitigation and correction schemes employed in the SSS products to reduce the impact of RFI might introduce other errors. Other contributors to the seasonal biases in satellite SSS are also possible.

The RFI sources and strengths are not constant, which complicates the effort of spinning down the causes. Near-realtime RFI maps for the SMAP satellite are produced using the algorithm developed by Piepmeier et al. (2014; 2016) and are available at (https://salinity.oceansciences.org/smap-radiometer.htm). These maps show that the strength of the RFI signals in L-band surface brightness temperatures change on seasonal timescales and has also substantial year-to-year variations. The nonstationary RFI signals, if not completely filtered out, could affect the seasonal cycle of satellite SSS retrievals. However, detecting the nonstationary RFI signals that have not been filtered out in satellite SSS is an ongoing effort because it depends on each individual retrieval algorithm. While detailing the effects of RFI on seasonal SSS phasing is beyond the scope of this paper, it is hoped that the discrepancies identified in this study would provide useful information for satellite retrieval teams to improve the accuracy of SSS in regions influenced by RFI.

4.2 Semiannual harmonic of SSS

Amplitudes of the estimated semiannual harmonic (A_2 in Eq.(1)) in the six products are shown in Figure 7. Argo and EN4 indicate that the semiannual component is small, far less than 0.1 pss, over most of the global ocean. Areas with significant semiannual component (amplitude > 0.3 pss) are in the near-coastal regions bordering large rivers, including the Amazon (the western tropical Atlantic), Congo and Niger (the equatorial eastern Atlantic), Mississippi (the northern Gulf of Mexico), Ganges-Brahmaputra (the Bay of Bengal), Yangtze River (the South China Sea), and Rio de la Plata estuary (at ~ 35°S on the Atlantic coast of South America). Satellite products are generally in good agreement with Argo and EN4 except for the coastal regions in the North Pacific with high amplitudes. In general, SMAP JPL has a stronger semiannual amplitude between 50–40°S than the other products. SMOS LOCEAN displays a zonal band of semiannual amplitude of 0.3 pss near 40°N mainly in the North Pacific, possibly related to the effect of RFI.

Phases of the estimated semiannual cycles (φ_2 in Eq. (1)) (Figure 8) show that all products agree well in the tropical ocean. Outside of the tropics, SMAP JPL and SMAP RSS have an overall in-phase relationship with Argo and EN4, whereas SMOS LOCEAN and SMOS BEC are generally out of phase with both in situ and SMAP products, particularly in the northern latitudes between 20–50°N.

4.3 Variances explained by the harmonic modes

The annual and semiannual cycles of SSS at each grid location were constructed using the respective first and second harmonic parameters, and the two cycles were then combined to reconstruct the seasonal variations. The R^2 values (Eq.(2)) and F-statistic (Eq. (3)) corresponding to the first and second harmonics and the total sum were computed respectively. R^2 values represent the percentage of the observed variance that can be accounted for by the given harmonic mode, and F values greater than 0.95 are considered statistically significant. Spatial patterns of R^2 corresponding to the annual and reconstructed total (annual + semiannual) seasonal cycles are shown in Figures 9 and 10, respectively, and the areas that have F values lower than 0.95 (not significant) are shaded (magenta). Basin averages of the R^2-based percentage contributions from all the three components (i.e. the annual, semiannual, and the reconstructed seasonal cycle) in the three individual basins (Pacific, Atlantic, and Indian) and the global ocean (50°S – 50°N) are summarized in Table 3.

The R^2 pattern of the annual harmonic (Figure 9) indicates that the percentage of the observed variance explained by the annual mode is largely similar to the annual amplitude. Areas where annual harmonic has a large contribution (>80%) to the observed variance are often areas of large annual amplitudes (> 0.2 pss) (Figure 5). Interestingly, the R^2 values for in situ products are generally greater than those for satellite products although the harmonic amplitude patterns are all similar. A similar result was also obtained by Bingham et al. (2021) in the tropics using mooring data as an in situ comparison. This is especially the case in the extratropical ocean where annual amplitudes in most areas are lower than 0.1 pss. For satellite products, the weak annual harmonic in the region corresponds to a low contribution to the total variance (<20%), whereas for in situ products, the weak annual harmonic in the region can still account for a substantial percentage of the total variance. This difference may reflect the impact of noise in data on the computation of R^2. As shown in Figure 4, the observed variance in in situ products is much smaller than that in the satellite products in the extratropical regions away from the marginal seas and the western boundary currents.

The R^2 values are increased by 10-20% almost everywhere over the globe when the semiannual harmonic was added to the annual harmonic to obtain the reconstructed seasonal cycle (Figure 10). The two harmonic modes account for most of the observed variance in EN4 and Argo, but they contribute much less to the satellite observed variances in the extratropical ocean where most of the R^2 values are small and not statistically significant. The differences between products can be better assessed when looking at the basin averages listed in Table 3. EN4 shows that, globally, 88% of the total SSS variance can be explained by the first two harmonic modes, with 72% of the variance coming from the annual harmonic and 16% from the semiannual harmonic. The partition of the annual and semiannual contributions is similar in the Pacific and Atlantic Oceans, but is tilted slightly toward the semiannual in the Indian Ocean due to the influence of monsoon forcing. By comparison, the first two harmonic modes in Argo contribute to about 80% of its total SSS variance, which is about 8% less than those in EN4 due to the weaker contribution of the annual harmonic in Argo. The four satellite products show that the annual and semiannual harmonics have percentage contributions similar to WOA in all basins but considerably lower than Argo and EN4.

4.4 Harmonic modes based on WOA

The first and second harmonics in the WOA salinity climatology were computed (Figure 11) and show clearly the advantages of the improved spatial resolution and increased data density over BL2002. The WOA annual harmonic has larger amplitudes and sharper amplitude bands (>0.3 pss) in regions of strong SSS variability, such as the ITCZ and SPCZ, river plumes, and coastal and marginal seas when compared to BL2002. The annual phase also shows considerable improvement over BL2002 in representing the refined zonal phase structures in the tropical ocean. For instance, the WOA annual phase has a thin band at the equator in the central and eastern Pacific that shows the SSS has its maximum in May-June. This band was not present in BL2002. Several other narrow zonal phase bands were also missed in BL002, including the bands of March-April phasing located on the equatorward edges of the subtropical Smax in the Pacific and Atlantic (about 20–25°N in the northern basins and 15–5°S in the southern basins). The semiannual harmonic pattern was also included in BL2002. The semiannual mode estimated from WOA bears a large similarity to Argo and EN4 (Figures 7-8 (e)-(f)).

4.5 Long-term perspective of the three-year based harmonic patterns

The improved representation of fine-scale features in the WOA provides a valid benchmark for assessing the long-term perspective of the three-year based harmonic modes presented above. In particular, it would be interesting to see whether the fine-scale features in the satellite harmonic modes are due to the use of a short period or replica of the climatological norms. Specifically, it would be interesting to know whether the three-year based seasonal cycle of SSS could be affected by potential spatiotemporal aliasing in regions that feature small-scale SSS variability such as the coastal oceans and river plumes.

The comparison of the first and second harmonics (Figures 5-8 and 11) indicates that the six recent SSS products, despite having only a three-year data span, are capable of reproducing all the main climatological features in WOA. These features include the SSS annual and semiannual amplitudes in open and coastal regions under direct freshwater influences, e.g. rainfall and/or river discharge, the narrow zonal bands of annual phasing in the tropical and southern oceans, and the annual phasing in the northwest Pacific and Atlantic. Satellite products compare well with WOA on the two harmonic amplitude patterns, and they also agree well with WOA on the phase distribution patterns at all latitudes except for the latitudes bands 20–40°N. The in situ products, particularly Argo, also show similar amplitude and phase patterns as the WOA.

WOA is a 60+ year climatology and so many modes of natural climate variability should be smoothed out on such a long time scale, whereas the satellite and in situ products over the 2016-2018 time period could be skewed by natural variability. For instance, the early 2016 was marked by the weakening of the strong El Niño of 2015/16 with a transition to El Niño-Southern Oscillation (ENSO) neutral phase, and the later 2017 and early 2018 were featured by a moderate La Niña. One noticeable difference is that the annual amplitude of the SSS associated with the ITCZ in the western equatorial Pacific (140ºE – 180) is weaker in the WOA than in the satellite (except SMOS BEC) and in situ (Argo and EN4) products (Figures 5 &11). This difference may reflect a La Niña influence on the three-year time series.

Satellite products reveal the importance of having a fine-enough spatiotemporal resolution for depicting the three narrow zonal bands of SSS annual amplitude of 0.4 – 0.5 pss in the far eastern equatorial Pacific fresh pool (110–80°W, 0–10°N) (Alory et al. 2012). These SSS amplitude bands result from SSS seasonal changes associated with the ITCZ (centered at ~10°N), the Costa Rica dome (~ 5°N), and the equatorial cold tongue (~ the equator). The ability to resolve the fine details of different SSS processes in the region is an excellent example of the advantages of satellite SSS remote sensing. Neither Argo nor EN4 are able to fully capture the spatial distinctions between the three mesoscale features. WOA is able to validate the climatological aspect of these three bands. However, long record of historical in-situ data could not guarantee near-uniform sampling or homogenous spatial coverage. A longer satellite data record is needed to determine the time-mean shape and magnitude of the meso- and frontal-scale SSS features.

Satellite products also show the advantages of remote sensing in detecting the SSS semiannual amplitude in the coastal regions influenced by river plumes (Figures 7 and 11b), the marginal seas, and the eastern equatorial Pacific where the three SSS bands are located. These semiannual amplitudes are evident in WOA but with blurry structures and limited details. Argo is a better version of EN4 and WOA in this regard, though the details are still lacking and there are no Argo observations in coastal regions.

4.6 Quantification of the deviations from WOA

Most of the dominant harmonic features are zonally oriented. To evaluate the deviation of the three-year based harmonic analysis from WOA, the amplitude, phase, and R^2 of the first and second harmonics in each product were zonally averaged and the WOA counterparts were subtracted. The latitudinal structures of the product-minus-WOA differences in harmonic parameters are shown in Figure 12.

The satellite products, except for SMOS BEC, tend to have slightly stronger annual and semiannual amplitudes than WOA, and more so in the Northern Hemisphere (Figures 12a-b). SMAP JPL is an outlier at higher latitudes (poleward of 40°N/S), where its amplitudes exceed WOA by 0.1 pss or greater. SMOS BEC has considerably weaker harmonic amplitudes in the tropical latitudes. On the other hand, Argo amplitudes are slightly weaker than WOA, and EN4 is more or less on the same level as WOA.

The two in situ products show generally good agreement with WOA on the annual harmonic phases, but less so on the semiannual harmonic phases (Figures 12c-d). The satellite products are less comparable. While SMAP JPL deviates from the WOA annual phase by ~ ± 40 days in mid and high latitudes, SMAP RSS and SMOS LOCEAN have large differences (~ ± 60 days) from WOA semiannual phases in the southern latitudes. SMOS BEC is least comparable to WOA in both harmonic phases.

The R^2 mean differences produce an interesting pattern. Although the R^2 values in Argo and EN4 are seen to be higher than those in satellite products (Figure 10), the fact that they are also higher than those in WOA is unexpected. The annual harmonic explains 10 – 20% more observed variance in the respective data product despite the relatively weaker annual amplitude (Figure 12a). One sensible explanation is the lower noise level (or a higher level of smoothness) in the two in situ products (Figure 5), which may be related to the coarser spatiotemporal sampling resolution and/or less nonseasonal variance during the three-year period. The data base for WOA does not have uniform sampling nor homogenous spatial coverage, and the six-decade long record encompasses a broad range of variability. WOA would have much greater sampling coverage than either Argo or EN4 products, as WOA would contain almost all the data used in the Argo and EN4 products plus all historical data. In addition, the 0.25º WOA fields were objectively analyzed on the 0.25º×0.25º resolution, whereas the Argo and EN4 products are on 1º×1º resolution but were interpolated down to 0.25º×0.25º resolution in computing R^2. These factors all contribute to the nonseasonal variance when calculating R^2, lowering the percentage of observed variance that can be explained by the harmonic modes. Thus, the coarser-resolution in situ products may underrepresent the full range of high-frequency small scale SSS variability when data record is short, which could enlarge the SSS explained variance by annual harmonic.

The global averages of the mean differences in amplitude, phase, and R^2 for annual and semiannual harmonics are summarized in Figure 13. The error bars represent one standard deviation from the zonal mean. The amplitude differences for the annual and semiannual harmonics (Figure 13a) show that satellite products except for SMOS BEC, have larger amplitudes than the WOA and in situ products. The phase differences for the annual harmonic (Figure 13b) are mostly small except for SMOS BEC that lags WOA by about 10 days. The phase differences for the semiannual harmonic are larger, with SMOS LOCEAN and SMAP JPL leading WOA by more than 10 days. The R^2 differences of the annual harmonic (Figure 13c) show that SMAP JPL and SMOS RSS are more or less on the same level as those in the WOA but are higher than SMOS LOCEAN and SMOS BEC and lower than Argo and EN4.

4.7 Characterization of Smin and Smax

Dominant features in the study domain between 50°S and 50°N are the Smin in the tropics and the Smax in the northern and southern subtropics (Gordon et al., 2015). These features mirror closely the maxima and minima in the global E–P patterns (Schanze et al., 2010;

Schmitt 2008; Yu et al. 2020), with the Smax regions supplying (net) water to the atmosphere and the Smin regions receiving (net) water from the atmosphere. Longer-term changes of seasonal SSS in these regions may shed an important light on the changes in the water cycle (e.g. Gordon et al., 2015; Reagan et al. 2018). For instance, there is evidence that the salinity contrast between the Smax and Smin values has increased since 1950 as the water cycle has intensified under global warming (e.g. Vinogradova and Ponte 2017; Cheng et al. 2020). These changes in SSS extrema affect the ocean processes not only in the near-surface layer but also in the ocean interior. The Smax area is where the near-surface waters are subducted to the permanent thermocline during late winter to form the subtropical underwater (STUW) in the upper 500 meters (O'Connor et al 2005). The subducted waters are advected away from the formation sites by the interior ocean circulation, spreading the water cycle change signals along their pathways (Qu et al. 2013; Katsura et al. 2013). A recent study has shown a volume increase of the STUW in the North Atlantic as a result of the poleward shift of the Smax center in recent decades (Yu et al. 2018). Given the climatic significance of the SSS extrema, the accuracy of SSS retrievals in these regions is of great importance.

The seasonality of the tropical Smin and the subtropical Smax are characterized using the estimated annual and semiannual harmonics. Amplitudes of annual and semiannual harmonics from the six products were averaged over the nine Smin and Smax boxes (Figure 3a and Table 4). The amplitude and seasonal range of the reconstructed SSS seasonal cycle of SSS for the respective boxes is summarized in Figure 14. For the boxes located in the open ocean away from monsoon-influenced regions, the seasonal range of SSS is mostly about ±0.05 pss in the subtropical Smax regime, but greater than ±0.25 in the tropical Smin regime. The seasonal amplitude of SSS is larger in the precipitation-dominated tropics than the evaporation-dominated subtropics. The differences in amplitude between the Smin and Smax regimes underline the different effects of evaporation and precipitation on the stability of the water column (Yu 2010). Evaporation increases SSS. If the SST change is not considered, this causes an increase of surface density, leading to a destabilization of the upper-ocean stratification and convective mixing of surface waters. Hence, evaporation-induced surface salinification cannot stay long. In contrast, precipitation reduces SSS. The reduced surface density increases surface buoyancy and stabilizes the upper-ocean stratification that allows the rain-induced fresh surface water to last possibly long enough to be observed before being destroyed by other processes such as wind-induced vertical mixing (Drushka et al. 2019). Such an effect is expected to be more significant under low-wind conditions. This study shows that although the harmonic amplitudes tend to be small in the Smax regions, they are detectable with the datasets used in the analysis.

5. Summary and discussion

SSS records with sufficient seasonal resolution over much of the global ocean have become available in the past 15 years thanks to the advent of the Argo profiling floats and L-band passive microwave remote sensing. This study utilized six SSS data products from the recent satellite and in situ platforms to assess the SSS seasonality in the global ocean between 50°S – 50°N. Harmonic analysis was applied to four 0.25° satellite products (SMAP JPL, SMAP RSS, SMOS LOCEAN, and SMOS BEC) and two 1° in situ products (Argo and EN4) between 2016-2018 to determine seasonal harmonic patterns. The 0.25° World Ocean Atlas (WOA) version 2018 was referenced to help assess the long-term perspective of the harmonic patterns based on a three-year period.

The results show that the annual harmonic is the most characteristic feature of the seasonal cycle, but the semiannual harmonic is not negligible, particularly in the Northern Indian Ocean under the influence of monsoonal circulation and the near coastal regions bordering large rivers, including the Amazon (the western tropical Atlantic), Congo and Niger (the equatorial eastern Atlantic), Mississippi (the northern Gulf of Mexico), and Ganges-Brahmaputra (the Bay of Bengal). When the two harmonics are combined to reconstruct the seasonal cycle, the semiannual harmonic is seen to modulate the annual harmonic. In the Bay of Bengal and the Arabian Sea, the semiannual amplitude is large enough to enhance the annual cycle if the two harmonics have the same phase, and weaken and broaden the annual cycle if the two have opposite phase.

The comparison of the first and second harmonics from the six recent SSS products with the WOA indicates that the products, despite having only a three-year data span, are capable of producing all essential climatological features of the WOA. These features include the SSS annual and semiannual amplitudes in open and coastal regions under direct freshwater influences, e.g. rainfall and/or river discharge, the narrow zonal bands of annual phasing in the tropical and southern oceans, and the northeast-southwest-oriented bands of annual phasing in the northwest Pacific and Atlantic. The satellite products, except for SMOS BEC, compare well with WOA on the annual and semiannual harmonic amplitude patterns, and they also agree well with WOA on the phase distribution patterns at all latitudes except for the bands 20–40°N where three products have a biased seasonal SSS phasing. Among the six products, SMOS BEC is least comparable with WOA.

R^2 values were computed to determine the percentage of the SSS observed variance that can be explained by the annual and semiannual harmonic respectively. It is found that the R^2

values vary with the type of product. The R^2 values for annual harmonic are relatively lower in satellite products, at about 49– 58%, but are higher in in situ products, at about 66 – 72 % (Bingham et al. 2021). The R^2 values for the semiannual harmonic are more in a more narrow range, at about 15 – 19% in all products. The large spread in the explained variance by the annual harmonic reflects a large disparity in nonseasonal variance (or noise) in products. Satellite products are capable of capturing sharp SSS features on meso- and frontal scales and the patterns agree well with WOA. These products are, however, subject to the impacts of radiometric noises and are algorithm dependent. The coarser-resolution in situ products may underrepresent the full range of high-frequency small scale SSS variability when data record is short, which may have enlarged the SSS explained variance by the annual harmonic.

The Smax and Smin regions provide important linkages between the ocean and the water cycle, with the Smax regions supplying (net) water to the atmosphere and the Smin regions receiving (net) water from the atmosphere. Given the climatic significance of the SSS extrema, the accuracy of SSS retrievals in these regions is of great importance. Although the harmonic amplitudes tend to be small in the Smax regions, this study shows that they are detectable with the datasets used in the analysis. The amplitude of seasonal SSS is approximately 0.05 pss in the Smax regions, but greater than 0.25 pss in the Smin regions.

Finally, it is worth pointing out that, in coastal oceans and marginal seas where in-situ measurements are sparse and where satellite SSS are subject to potential contamination by land signals, dedicated regional analyses are necessary to better understand the seasonal cycle of SSS and the potential limitations of the in situ and satellite salinity observing systems.

Acknowledgements

L.Yu was funded by NASA Ocean Salinity Science Team (OSST) activities through Grant 80NSSC18K1335. FMB was funded by the NASA OSST through grant 80NSSC18K1322. E. P. Dinnat was funded by NASA through grant 80NSSC18K1443. Data producers for the following satellite SSS datasets are sincerely thanked: CNES-IFREMER Centre Aval de Traitement des Données SMOS (CATDS) for the SMOS LOCEAN L3 Debiased products (https://www.catds.fr/Products/Available-products-from-CEC-OS/CEC-Locean-L3-Debiased-v4), the Barcelona Expert Center (BEC) for the SMOS BEC global SSS products (http://bec.icm.csic.es/ocean-global-sss/), the SMAP JPL and RSS products (https://podaac.jpl.nasa.gov/SMAP). We also acknowledge the following in situ gridded products: Argo (http://sio-argo.ucsd.edu/RG_Climatology.html), EN4 (https://www.metoffice.gov.uk/hadobs/en4/), and the WOA 2018 climatology (https://www.nodc.noaa.gov/cgi-bin/OC5/woa18/woa18.pl)

References

Abe, H., N. Ebuchi, N., H. Ueno, H. Ishiyama, and Y. Matsumura, 2019: Aquarius reveals eddy stirring after a heavy precipitation event in the subtropical North Pacific. *J Oceanogr* **75,** 37–50. https://doi.org/10.1007/s10872-018-0482-0

Alory, G., C. Maes, T. Delcroix, N. Reul, and F. Illig, 2012. Seasonal dynamics of sea surface salinity off Panama: The far Eastern Pacific Fresh Pool, *J. Geophys. Res. Oceans*, **117**, C04028, doi:10.1029/2011JC007802.

Bingham, F. M., G. R. Foltz, M. J. McPhaden, 2010. Seasonal cycles of surface layer salinity in the Pacific Ocean. *Ocean Sci*., **6**, 775–787, https://doi.org/10.5194/os-6-775-2010.

Bingham, F. M., G. R. Foltz, and M. J. McPhaden, 2012. Characteristics of the seasonal cycle of surface layer salinity in the global ocean. *Ocean Science*, **8**(5), 915.

Bingham, F. M. and T. Lee, 2017. Space and time scales of sea surface salinity and freshwater forcing variability in the global ocean (60°S– 60°N). *J. Geophys. Res. Oceans*, **122**, 2909–2922, doi:10.1002/ 2016JC012216.

Bingham, F. M., S. Brodnitz, and L. Yu, 2021: Sea surface salinity seasonal variability in the tropics from satellites, in situ compilations and mooring observations. *Remote Sens.* 13(1), 110; https://doi.org/10.3390/rs13010110.

Boutin, J., P. Waldteufel, N. Martin, G. Caudal, E. Dinnat, 2004. Salinity retrieved from SMOS measurements over Global Ocean: Imprecisions due to surface roughness and temperature uncertainties. *J. Atmos. Ocean. Technol.*, **21**, 1432–1447. doi:10.1175/1520-0426(2004)021<1432:SSRFSM>2.0.CO;2.

Boutin, J., Y. Chao, Y., W. E. Asher, *et al.* 2016. Satellite and in situ salinity: understanding near- surface stratification and sub-footprint variability. *Bull. Am. Meteorol. Soc*. **97**(10). https://doi.org/10.1175/BAMS-D-15-00032.1.

Boutin, J, J. L. Vergely, S. Marchand, F. D'Amico, A. Hasson, N. Kolodziejczyk, N. Reul, G. Reverdin, and J. Vialard, 2018. New SMOS sea surface salinity with reduced systematic errors and improved variability. *Remote Sens. Environ*. **214**, 115–134.

Boutin J., J.-L.Vergely, C. Thouvenin-Masson, A. Supply, D. Khvorostyanov, 2019. SMOS SSS L3 maps generated by CATDS CEC LOCEAN. debias V4.0. SEANOE., https://doi.org/10.17882/52804.

Boyer, T. P., and S. Levitus, 1994. Quality control and processing of historical oceanographic temperature, salinity, and oxygen data, NOAA Tech. Rep. NESDIS 81, U.S. Govt. Print. Off., Washington, D. C., 64 pp.

Boyer, T. P. and S. Levitus, 2002. Harmonic Analysis of Climatological Sea Surface Salinity. *J. Geophys. Res.,* **107**(C12), doi:10.1029/2001JC000829.

Boyer, T. P., M. E. Conkright, S. Levitus, D. Johnson, J. Antonov, T. O'Brien, C. Stephens, and R. Gelfeld, 1998. World Ocean Database 1998, vol. 5, Temporal Distribution of Ocean Station Data (Bottle) Temperature Profiles [CD-ROMs], 108 pp., NOAA Atlas NESDIS 22, U.S. Govt. Print. Off., Washington, D. C.

Bruce, J. G., G. D. R. Johnson, and J. C. Kindle, 1994. Evidence for eddy formation in the eastern Arabian Sea during the northeast monsoon. *J. Geophys. Res.*, **99**(C4): 7 651–7 664, http://dx.doi.org/10.1029/94JC00035.

Camara, I., N. Kolodziejczyk, J. Mignot, A. Lazar, and A. T. Gaye, 2015. On the seasonal variations of salinity of the tropical A tlantic mixed layer. *J. Geophys. Res. Oceans*, **120**, 4441– 4462, doi:10.1002/2015JC010865.

Chao, Y., J. D. Farrara, G. Schumann, K. M. Andreadis, D. Moller, 2015. Sea surface salinity variability in response to the Congo river discharge Cont. *Shelf Res.* **99**, 35–45. https://doi.org/10.1029/2010JC006937.

Chen, G., L. Peng, and C. Ma, 2018: Climatology and seasonality of upper ocean salinity: A three-dimensional view from Argo floats. *Clim. Dyn.,* **50,** 2169–2182. https://doi.org/10.1007/s00382-017-3742-6

Cheng, L., K. E. Trenberth, N. Gruber, J. P. Abraham, J. T. Fasullo, G. Li, M. E. Mann, X. Zhao, and J. Zhu, 2020. Improved Estimates of Changes in Upper Ocean Salinity and the Hydrological Cycle, *J. Clim.*, *33*(23), 10357-10381. https://doi.org/10.1175/JCLI-D-20-0366.1.

Cherniavskaia, E., I. Sudakov, K. Golden, C. Strong, and L. Timokhov, 2018. Observed winter salinity fields in the surface layer of the Arctic Ocean and statistical approaches to predicting large-scale anomalies and patterns. *Annals of Glaciology,* **59**, 83-100. doi:10.1017/aog.2018.10.

D'Addezio, J. M., B. Subrahmanyam, E. S. Nyadjro, and V. S. N. Murty, 2015. Seasonal variability of salinity and salt transport in the Northern Indian ocean. *J. Phys. Oceanogr.*, **45**, 1947–1966.

da Silva, C. E., and R. M. Castelao, 2018. Mississippi River plume variability in the Gulf of Mexico from SMAP and MODIS-Aqua observations. *J. Geophys. Res. Oceans*, **123**, 6620–6638. https://doi.org/10.1029/2018JC014159

Delcroix, T., C. Hénin, V. Porte, and P. Arkin, 1996. Precipitation and sea-surface salinity in the tropical Pacific Ocean, *Deep-Sea Res.*, **43**, 1123– 1141.

Delcroix, T., M. J. McPhaden, A. Dessier, and Y. Gouriou, 2005. Time and space scales for sea surface salinity in the tropical oceans, *Deep-Sea Res.,* **52**(5), 787–813.

Dessier, A., and J. R. Donguy, 1994. The sea surface salinity in the tropical Atlantic between 10S and 30N – Seasonal and interannual variations (1977–1989). *Deep Sea Res., Part I*, **41**, 81–100.

Dinnat, E., D. Le Vine, J. Boutin, T. Meissner, and G. Lagerloef, 2019. Remote sensing of sea surface salinity: Comparison of satellite and in situ observations and impact of retrieval parameters. *Remote Sens.* **11**, 750. https://doi.org/10.3390/rs11070750.

Dong, S., S. L. Garzoli, and M. Baringer, 2009. An assessment of the seasonal mixed layer salinity budget in the Southern Ocean. *J. Geophys. Res. Oceans*, **114**, C12001. https://doi.org/10.1029/2008JC005258

Donguy, J. E., and G. Meyers, 1996. Seasonal variations of sea surface salinity and temperature in the tropical Indian Ocean. *Deep Sea Res., Part I*, **43**, 117– 138.

Drucker, R., and S. C. Riser, 2014. Validation of Aquarius sea surface salinity with Argo: Analysis of error due to depth of measurement and vertical salinity stratification. *J. Geophys. Res. Oceans*, **119**, 4626–4637, doi:10.1002/ 2014JC010045

Drushka, K., W.E. Asher, A.T. Jessup, E.J. Thompson, S. Iyer, and D. Clark. 2019. Capturing fresh layers with the surface salinity profiler. Oceanography 32(2):76–85, https://doi.org/10.5670/ oceanog.2019.215.

Entekhabi, D., E. G. Njoku, P. E. O'Neill, *et al.* **2010**. The soil moisture active passive (SMAP) mission. *Proc. IEEE,* **98**, 704–716. doi: 10.1109/JPROC.2010.2043918.

Foltz, G. R., and M. J. McPhaden, 2008. Seasonal mixed layer salinity balance of the tropical North Atlantic Ocean, *J. Geophys. Res.*, **113**, C02013, doi:10.1029/2007JC004178.

Fore, A., S. Yueh, W. Tang, and A. Hayashi, 2020. JPL SMAP Ocean Surface Salinity Products [Level 2B, Level 3 Running 8-day, Level 3 Monthly], Version 4.3 validated release. Jet Propulsion Laboratory, Pasadena, CA, USA.

Fournier, S., T. Lee, and M. M. Gierach, 2016. Seasonal and interannual variations of sea surface salinity associated with the Mississippi River plume observed by SMOS and Aquarius. *Remote Sens. Environ.*, **180**, 431-439.

Fournier, S., J. Vialard, M. Lengaigne, T. Lee, M. Gierach, 2017a. Modulation of the Ganges-Brahmaputra river plume by the Indian Ocean Dipole and eddies inferred from satellite observations. *J. Geophys. Res. Oceans*, **122**. https:// doi.org/10.1002/2017JC013333.

Fournier, S., D. Vandemark, L. Gaultier, T. Lee, B. Jonsson, M. Gierach, 2017b. Interannual variation in offshore advection of Amazon-Orinoco plume waters: observations, forcing mechanisms, and impacts. *J. Geophys. Res. Oceans*, **122**. https://doi.org/10.1002/2017JC013103.

Fournier, S., T. Lee, W. Tang, M. Steele, E. Olmedo, 2019. Evaluation and intercomparison of SMOS, Aquarius, and SMAP sea surface salinity products in the Arctic Ocean. *Remote Sens.* **11**, 3043, doi:10.3390/rs11243043.

Fournier, S., & Lee, T. (2021). Seasonal and Interannual Variability of Sea Surface Salinity Near Major River Mouths of the World Ocean Inferred from Gridded Satellite and In-Situ Salinity Products. Remote Sensing, 13(4), 728.

Garcia-Eidell, C., J. C. Comiso, E. Dinnat, and L. Brucker, 2017. Satellite observed salinity distributions at high latitudes in the Northern Hemisphere: A comparison of four products. *J. Geophys. Res. Oceans*, **122**(9), 7717–7736. https://doi.org/10.1002/2017JC013184.

Garcia-Eidell, C., J. C. Comiso, E. Dinnat, and L. Brucker, 2019. Sea surface salinity distribution in the southern ocean as observed from space. *J. Geophys. Res. Oceans,* **124**(5), 3186–3205. https://doi.org/10.1029/2018JC014510.

Gelderloos, R., F. Straneo, and C. A. Katsman, 2012: Mechanisms behind the Temporary Shutdown of Deep Convection in the Labrador Sea: Lessons from the Great Salinity Anomaly Years 1968–71. *J. Climate*, **25**, 6743–6755, https://doi.org/10.1175/JCLI-D-11-00549.1.

Gierach, M., J. Vazquez-Cuervo, T. Lee, V. M. Tsontos, 2013. Aquarius and SMOS detect effects of an extreme Mississippi River flooding event in the Gulf of Mexico. *Geophys. Res. Lett.* **40**(19), 5188–5193. https://doi.org/10.1002/grl.50995.

Good, S. A., M. J. Martin, and N. A. Rayner, 2013. EN4: Quality controlled ocean temperature and salinity profiles and monthly objective analyses with uncertainty estimates. *J. Geophys. Res. Oceans*, **118**, 6704– 6716. https://doi.org/10.1002/2013JC009067.

Gordon, A.L., C.F. Giulivi, J. Busecke, and F.M. Bingham. 2015. Differences among subtropical surface salinity patterns. *Oceanography,* **28**(1):32–39, https://doi.org/10.5670/oceanog.2015.02.

Greene, C. H., 2013. Towards a more balanced view of marine ecosystems. *Fish Oceanogr,* **22**, 140-142. doi:10.1111/fog.12006.

Grodsky, S.A., G. Reverdin, J. A. Carton, V. J. Coles, 2014. Year-to-year salinity changes in the Amazon plume: contrasting 2011 and 2012 Aquarius/SAC-D and SMOS satellite data. *Remote Sens. Environ.* **140**, 14–22. https://doi.org/10.1016/j.rse.2013. 08.033.

Grodsky, S.A., N. Reul, B. Chapron, J. A. Carton, and F. O. Bryan, 2017. Interannual surface salinity in Northwest Atlantic shelf. *J. Geophys. Res. Oceans,* **122**(5), 3638–3659.

Hasson, A. E. A., T. Delcroix, and R. Dussin, 2013a. An assessment of the mixed layer salinity budget in the tropical Pacific Ocean: Observations and modelling (1990–2009). *Ocean Dyn.*, **63**(2–3), 179– 194, doi:10.1007/s10236-013-0596-2.

Hasson, A., T. Delcroix, and J. Boutin, 2013b. Formation and variability of the South Pacific Sea Surface Salinity maximum in recent decades. *J. Geophys. Res. Oceans,* **118**, doi:10.1002/jgrc.20367

Henocq, C., J. Boutin, G. Reverdin, F. Petitcolin, S. Arnault, and P. Lattes, 2010. Vertical Variability of Near-Surface Salinity in the Tropics: Consequences for L-Band Radiometer Calibration and Validation. *J. Atmos. Oceanic Technol.,* **27**, 192–209, https://doi.org/10.1175/2009JTECHO670.1

Jensen, T. G. 2001. Arabian Sea and Bay of Bengal exchange of salt and tracers in an ocean model, *Geophys. Res. Lett.*, **28**(20), 3967– 3970.

Jensen, M.F., J. Nilsson, and K. H. Nisancioglu, 2016. The interaction between sea ice and salinity-dominated ocean circulation: implications for halocline stability and rapid changes of sea ice cover. *Clim Dyn* **47,** 3301–3317. https://doi.org/10.1007/s00382-016-3027-5.

Johnson, B.K., F.O. Bryan, S.A. Grodsky, and J.A. Carton, 2016: Climatological Annual Cycle of the Salinity Budgets of the Subtropical Maxima. *J. Phys. Oceanogr.,* **46**, 2981–2994, https://doi.org/10.1175/JPO-D-15-0202.1.

Katsura, S., E. Oka, B. Qiu, and N. Schneider, 2013, Formation and subduction of North Pacific Tropical Water and their interannual variability, *J. Phys. Oceanogr.*, **43**(11), 2400– 2415.

Kerr, Y. H., P. Waldteufel, J.-P. Wigneron, *et al*. 2010. The SMOS L: New tool for monitoring key elements of the global water cycle. Proc. IEEE, **98**(5), 666-687. doi:10.1109/JPROC.2010.2043032.

Köhler, J., M.S. Martins, N. Serra, D. Stammer, 2015. Quality assessment of spaceborne sea surface salinity observations over the northern North Atlantic. *J. Geophys. Res. Oceans*, **120**, 94–112, doi:10.1002/2014JC010067.

Lagerloef, G., C. Swift, D. Le Vine, 1995. Sea surface salinity: the next remote sensing challenge. *Oceanography,* **8**(2), 44–50.

Le Vine, D., A. Saji, Y. H. Kerr, W. J. Wilson, N. Skou, S. Sobjaerg, 2005. Comparison of model predictions with measurements of galactic background noise at L-band. *IEEE Geosci. Remote Sens.,* **43**(9), 2018–2023. doi:10.1109/TGRS.2005.853190.

Levitus, S., 1986. Annual cycle of salinity and salt storage in the world ocean. *J. Phys. Oceanogr.,* **16**, 322–343.

Maes, C., and T. J. O'Kane, 2014. Seasonal variations of the upper ocean salinity stratification in the Tropics, *J. Geophys. Res. Oceans*, **119**, 1706– 1722, doi:10.1002/2013JC009366.

Martín-Neira, M., R. Oliva, I. Corbella, et al. 2016. SMOS instrument performance and calibration after six years in orbit. *Remote Sens. Environ.,* **180**, 19–39. https://doi.org/10.1016/j.rse.2016.02.036

Melnichenko, O.V., P. Hacker, F. Bingham, T. Lee, 2019. Patterns of SSS variability in the eastern tropical Pacific: intra-seasonal to inter-annual time-scales from seven years of NASA satellite data. *Oceanography*, **32**(2), 20-29, doi:10.5670/oceanog.2019.208.

Meissner, T., F. J. Wentz, A. Manaster, 2018: NASA/RSS SMAP Salinity: Version 3.0 Validated Release, Release Notes, Algorithm Theoretical Basis Document (ATBD), Validation, Data Format Specification. RSS Technical Report 091316. Available at http://data.remss.com/smap/SSS/Release_V4.0.pdf

Meissner, T., F. J. Wentz, A. Manaster, R. Lindsley, 2019: Remote Sensing Systems SMAP Ocean Surface Salinities [Level 2C, Level 3 Running 8-day, Level 3 Monthly], Version 4.0 validated release. Remote Sensing Systems, Santa Rosa, CA, USA. Available online at www.remss.com/missions/smap.

Melzer, B. A., and B. Subrahmanyam, 2015. Investigating decadal changes in sea surface salinity in oceanic subtropical gyres. *Geophys. Res. Lett.,* **42**, 7631–7638, doi:10.1002/2015GL065636.

Momin, I. M., A. K. Mitra, S. Prakash, D. K. Mahapatra, A. Gera, and E. N. Rajagopal, 2015. Variability of sea surface salinity in the tropical Indian Ocean as inferred from Aquarius and in situ data sets. *Int. J. Remote Sens.*, **36**(7), 1907-1920.

O'Connor, B. M., R. A. Fine, and D. B. Olson, 2005. A global comparison of subtropical underwater formation rates, *Deep Sea Res., Part I*, **52**(9), 1569– 1590.

Oliva, R., E. Daganzo-Eusebio, Y.H. Kerr, *et al*. 2012. SMOS radio frequency interference scenario: status and actions taken to improve the RFI environment in the 1400-1427- MHz passive band. *IEEE Trans. Geosci. Remote Sens.*, **50**(5), 1427-1439, doi:10.1109/TGRS.2012.2182775.

Olmedo, E., J. Martínez, A. Turiel, J. Ballabrera-Poy, M. Portabella, 2017. Debiased non-Bayesian retrieval: A novel approach to SMOS Sea Surface Salinity. *Remote Sens. Environ.,* **193**, 103-126, /doi:10.1016/j.rse.2017.02.023.

Piepmeier, J. R., J. T. Johnson, P. N. Mohammed, D. Bradley, C. Ruf, M. Aksoy, R. Garcia, D. Hudson, L. Miles, and M. Wong, 2014. Radio-frequency Interference Mitigation for the Soil Moisture Active Passive Microwave Radiometer. *IEEE Trans. Geosci. Remote Sen.* **52**(1), 761-775.

Piepmeier, J.R., P. Mohammed, G. De Amici, E. Kim, J. Peng, and C. Ruf, 2016. Soil Moisture Active Passive (SMAP) Project, Algorithm Theoretical Basis Document, SMAP L1B Radiometer Brightness Temperature, Data Product: L1B_TB (Rev. B), NASA Goddard Space Flight Center, 83p. available from https://ntrs.nasa.gov/citations/20160003317.

Piola, A. R., R. P. Matano, E. D. Palma, O. O. Möller, and E. J. D. Campos, 2005. The influence of the Plata River discharge on the western South Atlantic shelf. *Geophys. Res. Lett.*, **32**, L01603, doi:10.1029/2004GL021638.

Piracha, A., R. Sabia, M. Klockmann, L. Castaldo, and D. Fernández, 2019. Satellite-driven estimates of water mass formation and their spatio-temporal evolution. *Front. Mar. Sci.,* **6**(589), doi:10.3389/fmars.2019.00589.

Qu, T., S. Gao, and R. A. Fine, 2013. Subduction of South Pacific Tropical Water and its equatorward pathways as shown by a simulated passive tracer, *J. Phys. Oceanogr.*, **43**(8), 1551– 1565.

Rao, R. R., and R. Sivakumar, 2003. Seasonal variability of sea surface salinity and salt budget of the mixed layer of the north Indian Ocean. *J. Geophys. Res. Oceans*, **108**(C1), 3009, https://doi.org/10.1029/2001JC000907.

Reagan, J., T. Boyer, J. Antonov, and M. Zweng, 2014. Comparison analysis between Aquarius sea surface salinity and World Ocean Database in situ analyzed sea surface salinity. *J. Geophys. Res. Oceans*, **119**, 8122– 8140, doi:10.1002/2014JC009961.

Reagan, J., D. Seidov, and T. Boyer, 2018. Water Vapor Transfer and Near-Surface Salinity Contrasts in the North Atlantic Ocean. *Sci. Rep.* **8,** 8830. https://doi.org/10.1038/s41598-018-27052-6.

Ren, L., K. Speer, and E. P. Chassignet, 2011. The mixed layer salinity budget and sea ice in the Southern Ocean, *J. Geophys. Res.*, **116**, C08031, doi:10.1029/2010JC006634.

Reul, N., J. Tenerelli, B. Chapron, P. Waldteufel, 2007. Modelling sun glitter at L-band for the sea surface salinity remote sensing with SMOS. *IEEE Trans. Geosci. Remote Sens.,* **45**(7), 2073–2087. doi: 10.1109/TGRS.2006.890421.

Reul, N., Fournier, S., Boutin, J., Hernandez, O., Maes, C., Chapron, B., Alory, G., Quilfen, Y., Tenerelli, J., Morisset, S., Kerr, Y., Mecklenburg, S., Delwart, S., 2014. Sea sur- face salinity observations from space with the SMOS satellite: A new means to monitor the marine branch of the water cycle. *Surv. Geophys.* **35**(3), 681–722. https://doi.org/10.1007/s10712-013-9244-0.

Reul, N.. S. A. Grodsky, M. Arias, *et al.* 2020. Sea surface salinity estimates from spaceborne L-band radiometers: An overview of the first decade of observation (2010–2019). *Remote Sens. Environ.,* **242**, 111769, https://doi.org/10.1016/j.rse.2020.111769.

Riser, S. C. et al., 2016. Fifteen years of ocean observations with the global Argo array. *Nature Clim. Change,* 6, 145-153, https://doi.org/10.1038/NCLIMATE2872.

Roemmich, D., and J. Gilson, 2009. The 2004–2008 mean and annual cycle of temperature, salinity, and steric height in the global ocean from the Argo Program. *Prog. Oceanogr.,* **82**, 81–100.

Sasamal, S. K., 1990. High saline waters in Bay of Bengal. *Proc. Indian Acad. Sci. (Earth. Planet. Sci.)*, **99**, 367-381.

Schanze, J. J., R. W. Schmitt, and L. L. Yu, 2010. The global oceanic freshwater cycle: A state-of-the-art quantification. *J. Mar. Res.,* **68**(3), 569–595, doi:10.1357/002224010794657164.

Schmidtko, S., G. C. Johnson, and J. M. Lyman, 2013. MIMOC: A global monthly isopycnal upper-ocean climatology with mixed layers, J. *Geophys. Res. Oceans,* **118**, 1658–1672, doi:10.1002/jgrc.20122

Schmitt, R.W., 2008. Salinity and the global water cycle. *Oceanography*, **21**(1), 12–19. https://doi.org/10.5670/oceanog.2008.63.

Schott F, & McCreary J P. 2001. The monsoon circulation of the Indian Ocean. *Prog. Oceanogr.*, **51**(1), 1–123, http://dx.doi.org/10.1016/S0079-6611(01)00083-0.

Sena Martins, M., Serra, N., and Stammer, D. (2015), Spatial and temporal scales of sea surface salinity variability in the Atlantic Ocean, *J. Geophys. Res. Oceans*, 120, 4306– 4323, doi:10.1002/2014JC010649.

Shenoi, S. S. C., D. Shankar, and S. R. Shetye, 1999. On the sea surface temperature high in the Lakshadweep Sea before the onset of the southwest monsoon, *J. Geophys. Res.*, **104**(C7), 15703– 15712, doi:10.1029/1998JC900080.

SMOS-BEC Team, 2019: Global SMOS-BEC Debiased non-Bayesian SSS L3 and L4 Product Description. Barcelona Expert Centre, Spain, Technical note: BEC-SMOS-0007-QR version 1.0, available at: http://bec.icm.csic.es/doc/BEC-SMOS-0002-PD-SSS-Global.pdf, BEC 2019-07-15. Issue 1.0. pp.25.

Song, Y. T., T. Lee, J.-H. Moon, T. Qu, and S. Yueh (2015), Modeling skin- layer salinity with an extended surface- salinity layer, *J. Geophys. Res. Oceans*, 120, 1079–1095, doi:10.1002/ 2014JC010346.

Swift, C. T. 1980. Passive microwave remote sensing. *Bound.-Layer Meteor.,* **18,** 25–54.

Swift, C.T., McIntosh, R.E., 1983. Considerations for microwave remote sensing of ocean surface salinity. *IEEE Trans. Geosci. Remote Sens*. **21**, 480–491.

Talley, L.D. 2002. Salinity patterns in the ocean. In *Encyclopedia of Global Environmental Change (vol. 1): The Earth System.* Physical and Chemical Dimensions of Global Environmental Change. M.C. MacCracken and J.S. Perry, eds, John Wiley and Sons. pp. 629–640.

Tang, W., S. Yueh, D. Yang, A. Fore, A. Hayashi, T. Lee, S. Fournier, and B. Holt, 2018. The potential and challenges of using SMAP SSS to monitor Arctic Ocean freshwater changes. *Remote Sens.*, doi:10.3390/rs10060869, June 2018.

Tang, W.; Yueh, S.H.; Yang, D.; Mcleod, E.; Fore, A.; Hayashi, A.; Olmedo, E.; Martínez, J.; and Gabarró, C. 2020. The Potential of Space-Based Sea Surface Salinity on Monitoring the Hudson Bay Freshwater Cycle. *Remote Sens.* **12**, 873, doi:10.3390/rs12050873.

Vinogradova, N. T., and R. M. Ponte, 2013. Clarifying the link between surface salinity and freshwater fluxes on monthly to interannual time scales. *J. Geophys. Res. Oceans,* **118**, 3190– 3201. https://doi.org/10.1002/jgrc.20200.

Vinogradova, N. T., and R. M. Ponte, 2017: In search of fingerprints of the recent intensification of the ocean water cycle. *J. Climate*, **30**, 5513–5528, https://doi.org/10.1175/JCLI-D-16-0626.1.

Vinogradova, N., L. Tong, J. Boutin, *et al.* 2019. Satellite salinity observing system: Recent discoveries and the way forward. *Front. Mar. Sci.,* **6***,* 243, doi:10.3389/fmars.2019.00243.

Wilks, D.S. (1995) Statistical Methods in the Atmospheric Sciences. Academic Press, San Diego, 467 pp.

Wyrtki, K. 1965. The annual and semiannual variation of sea surface temperature in the North Pacific Ocean. *Limnol. Oceanogr.*, **10**, 307-313, doi: 10.4319/lo.1965.10.3.0307.

Yu, L. 2010. On Sea Surface Salinity Skin Effect Induced by Evaporation and Implications for Remote Sensing of Ocean Salinity. *J. Phys. Oceanogr.* **40,** 85–102, doi:10.1175/2009JPO4168.1.

Yu, L. 2011. A global relationship between the ocean water cycle and near-surface salinity. *J. Geophys. Res. Oceans*, **116**, C10025. https://doi.org/10.1029/2010JC006937

Yu, L., 2015. Sea-surface salinity fronts and associated salinity-minimum zones in the tropical ocean. *J. Geophys. Res. Oceans,* **120**(6), 4205–4225. doi:10.1002/2015JC010790.

Yu, L., Jin, X., Liu, H., 2018. Poleward shift in ventilation of the North Atlantic sub- tropical underwater. *Geophys. Res. Lett*. **45**, 258–266. https://doi.org/10.1002/ 2017GL075772.

Yu, L., 2020. Variability and Uncertainty of Satellite Sea Surface Salinity in the Subpolar North Atlantic (2010–2019). *Remote Sens.* **12**(13), 2092. https://doi.org/10.3390/rs12132092.

Yu, L., S.A. Josey, F.M. Bingham, and T. Lee, 2020. Intensification of the global water cycle and evidence from ocean salinity: a synthesis review. *Ann. N.Y. Acad. Sci.,* **1472**, 76-94. doi:10.1111/nyas.14354.

Yueh, S.H., West, R., Wilson, W.J., Li, F.K., Njoku, E.G., Rahmat-Samii, Y., 2001. Error sources and feasibility for microwave remote sensing of ocean salinity. *IEEE Trans. Geosci. Remote Sens.* **39**(5), 1049–1060.

Zweng, M. M., J. R. Reagan, D. Seidov, T. P. Boyer, R. A. Locarnini, H. E. Garcia, A. V. Mishonov, O. K. Baranova, K. Weathers, C. R. Paver, and I. Smolyar, 2018. *World Ocean Atlas 2018, Volume 2: Salinity.* A. Mishonov Technical Ed.; NOAA Atlas NESDIS 82, 50 pp. Available from https://www.nodc.noaa.gov/OC5/WOA/pubWOA.html.

List of Tables

Table 1. Main characteristics of the six products used in the study

Data Products	Version	Start Time	Resolution	Reference and data access site
SMAP JPL	v4.3	APR 2015	0.25°, monthly and 8-day running mean	Fore et al. (2016; 2019) https://podaac.jpl.nasa.gov/SMAP
SMAP RSS	v4.0	APR 2015	0.25°, monthly and 8-day running mean; 40-km and 70-km maps	Meissner et al. (2019a;b) https://podaac.jpl.nasa.gov/SMAP
SMOS LOCEAN	De-biased v4	JAN 2010	0.25°, 9-day and 18-day averaged mean	Boutin et al. (2018; 2019) ftp://ext-catds-cecos-locean:catds2010@ftp.ifremer.fr/
SMOS BEC	v2	FEB 2011	0.25°, Daily from 9 day objective analysis	Olmedo et al. (2017) sftp://becftp.icm.csic.es:27500
Argo	v2019	JAN 2004	1°, monthly	Roemmich and Gilson (2009) http://sio-argo.ucsd.edu/RG_Climatology.html
EN4	v4.2.1	JAN 1900	1°, monthly	Good et al. (2013) https://www.metoffice.gov.uk/hadobs/en4
WOA	v2018	climatology	0.25°, monthly	Zweng et al. (2018) https://www.nodc.noaa.gov/OC5/woa18

Table 2. Locations and abbreviated names of the nine boxes shown in Figure 3, along with product ensemble SSS mean and STD (spread) within the box.

Regime	**Box number**	**Abbreviated Name**	**Location**	**Mean SSS**
Smin Tropical	Box 1	Smin-Pac	5–15°N, 155–100°W	33.84 ± 0.09
	Box 2	Smin-Atl	3–13°N, 42–17°W	35.69 ± 0.03
	Box 3	Smin-BoB	5–20°N, 82–92°E	32.93 ± 0.07
Smax Northern Hemisphere Subtropical	Box 4	Smax-NPac	22–32°N, 160–220°E	35.12 ± 0.02
	Box 5	Smax-NAtl	20–30°N, 55–15°W	37.24 ± 0.03
	Box 6	Smax-AS	5–22°N, 55–70°E	36.16 ± 0.13
Smax Southern Hemisphere Subtropical	Box 7	Smax-SPac	14–24°S, 210–265°E	36.25 ± 0.03
	Box 8	Smax-SAtl	13–23°S, 38–18°W	37.16 ± 0.03
	Box 9	Smax-SInd	25–35°S, 60–110°E	35.70 ± 0.04

Table 3. R^2 values showing the percentage of the observed variance that can be explained by the annual and semiannual harmonics and the reconstructed seasonal cycle for the global ocean and the three basins

Basin	**Harmonic Mode**	**SMAP JPL**	**SMP RSS**	**SMOS LOCEAN**	**SMOS BEC**	**Argo**	**EN4**	**WOA**
Global (50°S-50°N)	Ann | Semi	55 | 18	58 | 17	50 | 19	49| 17	66 | 15	72 | 16	57 | 15
	Reconstructed	**73**	**74**	**70**	**67**	**80**	**88**	**72**
Pacific	Ann | Semi	56| 17	59 | 15	50 | 20	52 |17	69 | 13	75 | 14	57 | 15
	Reconstructed	**73**	**74**	**70**	**69**	**82**	**89**	**72**
Atlantic	Ann | Semi	61 | 16	58 | 17	53 | 18	47 | 18	67 | 14	72 | 15	59 | 14
	Reconstructed	**77**	**75**	**71**	**65**	**81**	**88**	**73**
Indian	Ann | Semi	48 | 22	52 | 19	47 | 21	47 | 18	47 | 18	67 | 19	55 | 17
	Reconstructed	**69**	**72**	**68**	**65**	**76**	**87**	**72**

Table 4. Amplitudes of the first (A_1) and second (A_2) harmonics in the nine boxes

<table>
<tr><th rowspan="2">Regime</th><th rowspan="2">Box Number</th><th>SMAP JPL</th><th>SMP RSS</th><th>SMOS LOCEAN</th><th>SMOS BEC</th><th>Argo</th><th>EN4</th><th>Ensemble Mean</th></tr>
<tr><th>A_1 | A_2</th><th>A_1 | A_2</th><th>A_1 | A_2</th><th>A_1 | A_2</th><th>A_1 | A_2</th><th>A_1 | A_2</th><th>A_1 | A_2</th></tr>
<tr><td rowspan="3">Smin Tropical regime</td><td>Box 1 (Smin-Pac)</td><td>0.24 | 0.05</td><td>0.25 | 0.05</td><td>0.24 | 0.05</td><td>0.17 | 0.02</td><td>0.26 | 0.05</td><td>0.23 | 0.03</td><td>0.23 ± 0.03 | 0.04 ± 0.01</td></tr>
<tr><td>Box 2 (Smin-Atl)</td><td>0.33 | 0.07</td><td>0.31 | 0.07</td><td>0.38 | 0.07</td><td>0.21| 0.01</td><td>0.28| 0.08</td><td>0.26| 0.06</td><td>0.30 ± 0.06 | 0.06 ± 0.03</td></tr>
<tr><td>Box 3 (Smin-BoB)</td><td>0.33 | 0.20</td><td>0.24 | 0.21</td><td>0.32 | 0.15</td><td>0.37 | 0.12</td><td>0.21 | 0.21</td><td>0.18 | 0.14</td><td>0.28 ± 0.08 | 0.17 ± 0.04</td></tr>
<tr><td rowspan="3">Smax NH regime</td><td>Box 4 (Smax-NPac)</td><td>0.08 | 0.01</td><td>0.01 | 0.02</td><td>0.02 | 0.06</td><td>0.01 | 0.03</td><td>0.04 | 0.01</td><td>0.02 | 0.01</td><td>0.03 ± 0.03 | 0.02 ± 0.02</td></tr>
<tr><td>Box 5 (Smax-NAtl)</td><td>0.12 | 0.01</td><td>0.04 | 0.02</td><td>0.03 | 0.02</td><td>0.00 | 0.01</td><td>0.06 | 0.02</td><td>0.06 | 0.02</td><td>0.05 ± 0.04 | 0.02 ± 0.01</td></tr>
<tr><td>Box 6 (Smax-AS)</td><td>0.23 | 0.09</td><td>0.24 | 0.06</td><td>0.17 | 0.05</td><td>0.11 | 0.04</td><td>0.20 | 0.08</td><td>0.21 | 0.07</td><td>0.19 ± 0.05 | 0.07 ± 0.02</td></tr>
<tr><td rowspan="3">Smax SH regime</td><td>Box 7 (Smax-SPac)</td><td>0.06 | 0.02</td><td>0.04 | 0.02</td><td>0.05 | 0.00</td><td>0.03 | 0.01</td><td>0.04 | 0.01</td><td>0.02 | 0.01</td><td>0.04 ± 0.01 | 0.01 ± 0.01</td></tr>
<tr><td>Box 8 (Smax-SAtl)</td><td>0.16 | 0.03</td><td>0.11 | 0.01</td><td>0.10 | 0.01</td><td>0.03 | 0.01</td><td>0.10 | 0.01</td><td>0.08 | 0.00</td><td>0.10 ± 0.04 | 0.01 ± 0.01</td></tr>
<tr><td>Box 9 (Smax-SInd)</td><td>0.05 | 0.03</td><td>0.07 | 0.03</td><td>0.03 | 0.05</td><td>0.04 | 0.01</td><td>0.05 | 0.00</td><td>0.05 | 0.02</td><td>0.05 ± 0.01 | 0.02 ± 0.02</td></tr>
</table>

Figure Captions

Figure 1. Time-mean SSS fields averaged over the period 2016-2018. (a) SMAP JPL, (b) SMAP RSS, (c) SMOS LOCEAN, (d) SMOS BEC, (e) Argo, and (f) EN4. The 35 pss isoline is drawn (thin gray contour)

Figure 2. Difference anomaly fields referenced to the WOA mean SSS. (a) SMAP JPL – WOA, (b) SMAP RSS – WOA, (c) SMOS LOCEAN – WOA, (d) SMOS BEC – WOA, (e) Argo – WOA, and (f) EN4 – WOA. In (e)-(f), the in situ products were interpolated on WOA 0.25° grids.

Figure 3. (a) Ensemble mean and (b) Standard deviation (STD) of the six mean SSS products. Numbered boxes are discussed in the text (e.g. Table 2). In (a), salinity value near each box is the product ensemble mean. Closed contours in boxes 4-9 are contours of the product ensemble mean shown near each box with each color denoting a different product.

Figure 4. Standard deviation (in pss) of monthly-mean SSS based on (a) SMAP JPL, (b) SMAP RSS, (c) SMOS LOCEAN, (d) SMOS BEC, (e) Argo, and (f) EN4.

Figure 5. Amplitude of the estimated annual harmonic (in pss) for (a) SMAP JPL, (b) SMAP RSS, (c) SMOS LOCEAN, (d) SMOS BEC, (e) Argo, and (f) EN4.

Figure 6. Phase of the estimated annual harmonic (month of the year of the maximum SSS) for (a) SMAP JPL, (b) SMAP RSS, (c) SMOS LOCEAN, (d) SMOS BEC, (e) Argo, and (f) EN4. The month shown indicates when maximum SSS is reached in the annual cycle.

Figure 7. Same as Figure 5 but for the estimated semiannual harmonic.

Figure 8. Same as Figure 6 but for the estimated semiannual harmonic. The cycle goes from January to June and repeats in July – December.

Figure 9. R^2 values (%) showing the percentage of the observed variance explained by annual harmonic. The F-statistic values less than 0.95 were considered not statistically significant and shaded in magenta.

Figure 10. Same as Figure 9 but for the seasonal cycle reconstructed from annual and semiannual harmonics.

Figure 11. The first and second harmonic modes estimated from WOA. Amplitude of (a) annual and (b) semiannual harmonic, and phase of (c) annual and (d) semiannual harmonic (the cycle goes from January to June and repeats in July – December).

Figure 12. Zonally averaged differences between product and WOA for the annual and semiannual parameters. Amplitude of (a) annual and (b) semiannual harmonic, phase of (c) annual and (d) semiannual harmonic, and R2 of (e) annual and (f) semiannual harmonic. A 15-point running mean was applied.

Figure 13. Global averages of the differences between SSS products and WOA in annual and semiannual parameters. (a) amplitude, (b) phase, and (c) R^2. . Error bars represent one standard deviation from zonal mean at each latitude.

Figure 14. Summary of the mean, standard deviation (bold-face numbers), and the seasonal ranges (light-face numbers) for each boxed region. The mean and standard deviation were computed as the product ensemble mean and spread (STD) (see Table 2). The seasonal ranges were based on the maximum and minimum estimated from the reconstructed time series averaged over the nine selected boxes (see Table 4). Color shading shows the ensemble mean SSS of the six products over the period of 2016-2018 (same as Figure 3a).

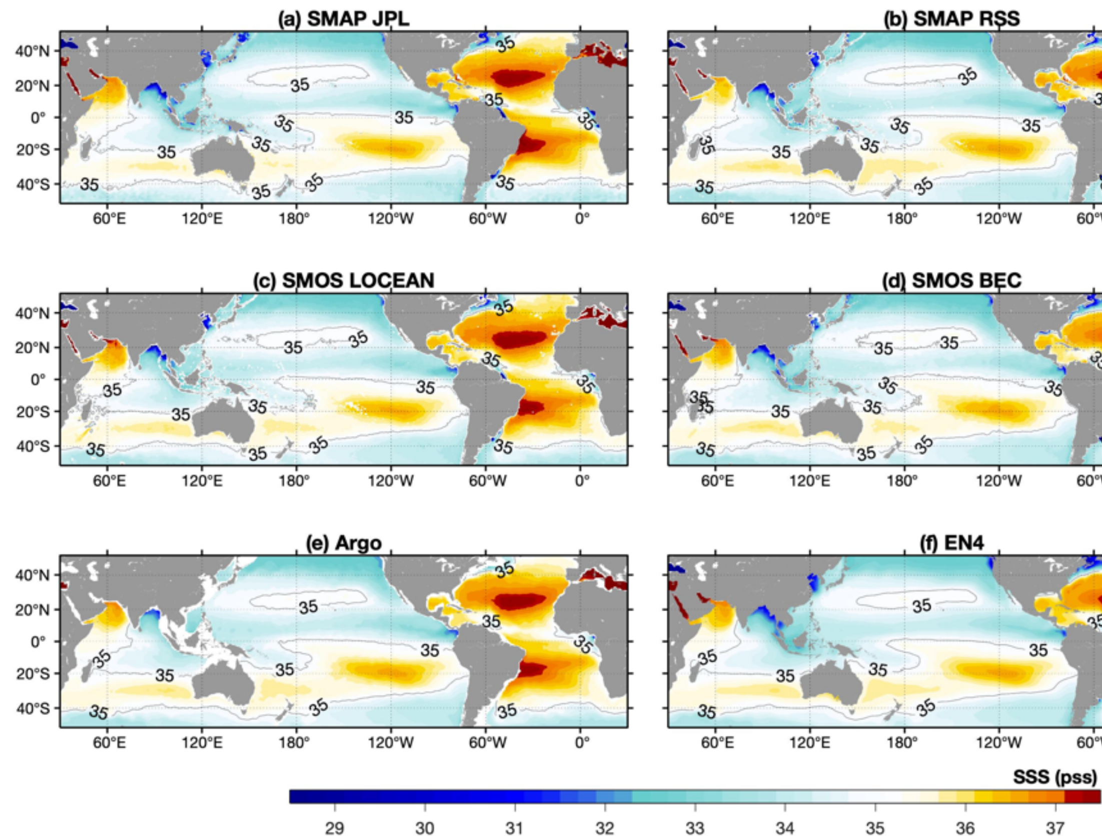

Figure 1. Time-mean SSS fields averaged over the period 2016-2018. (a) SMAP JPL, (b) SMAP RSS, (c) SMOS LOCEAN, (d) SMOS BEC, (e) Argo, and (f) EN4. The 35 pss isoline is drawn (thin gray contour).

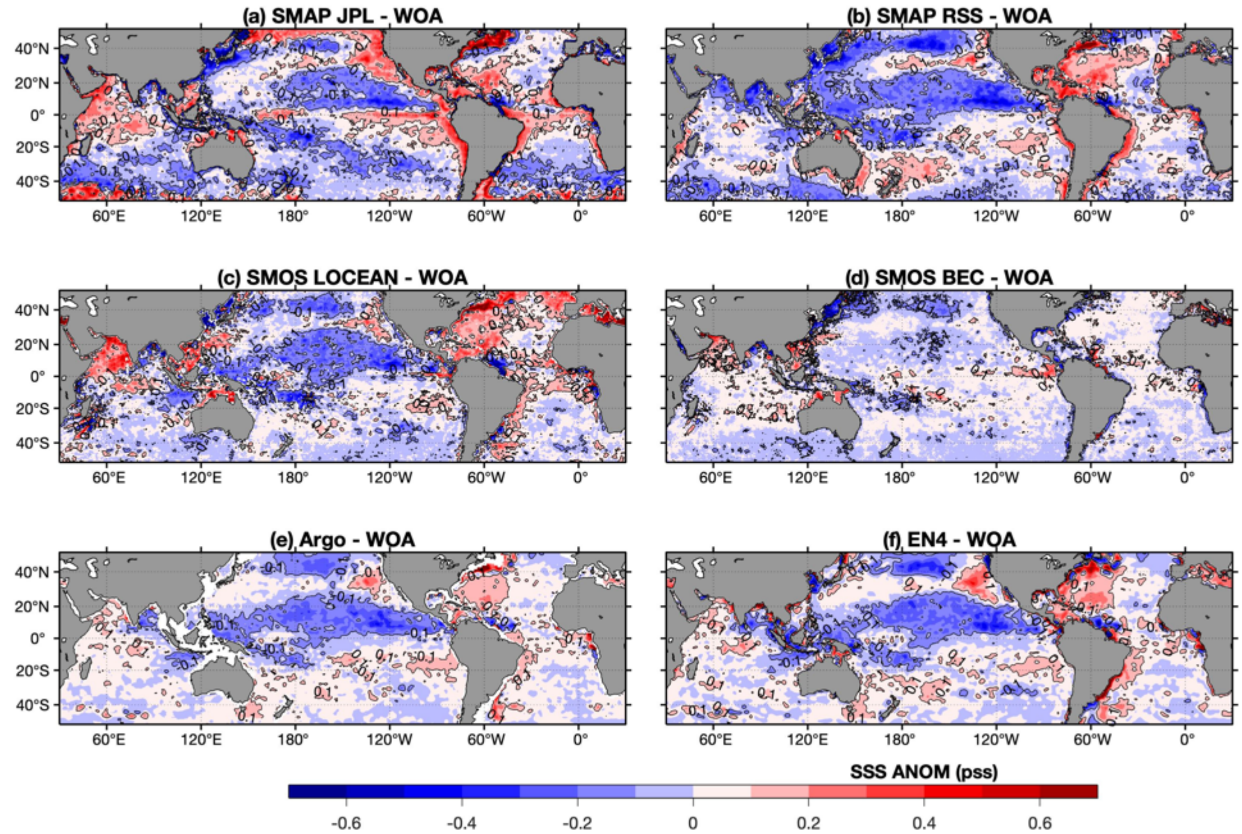

Figure 2. Difference anomaly fields referenced to the WOA mean SSS. (a) SMAP JPL – WOA, (b) SMAP RSS – WOA, (c) SMOS LOCEAN – WOA, (d) SMOS BEC – WOA, (e) Argo – WOA, and (f) EN4 – WOA. In (e)-(f), the in situ products were interpolated on WOA 0.25° grids.

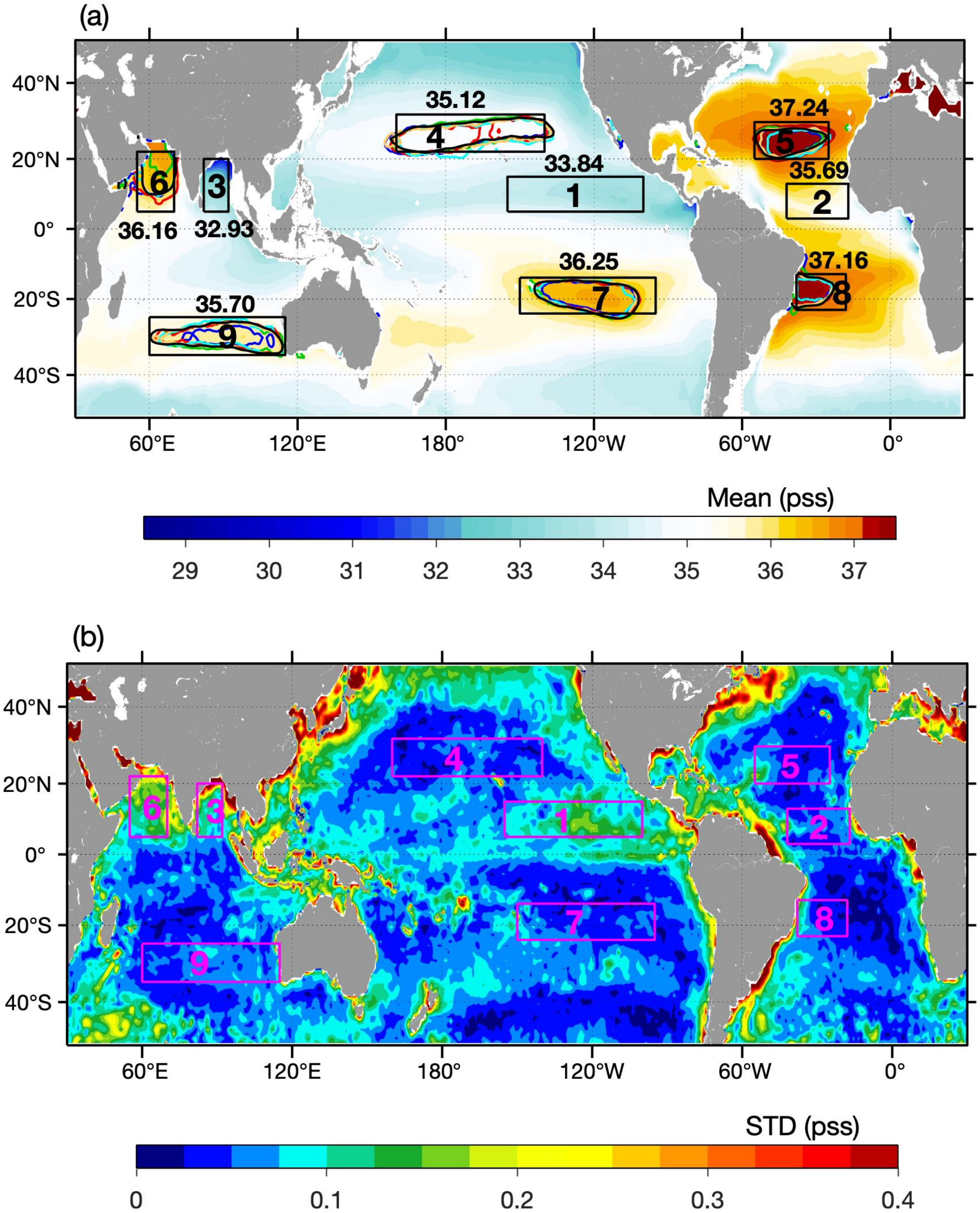

Figure 3. (a) Ensemble mean and (b) Standard deviation (STD) of the six mean SSS products. Numbered boxes are discussed in the text (e.g. Table 2). In (a), salinity value near each box is the product ensemble mean. Closed contours in boxes 4-9 are of the product ensemble mean shown near each box with each color denoting a different product.

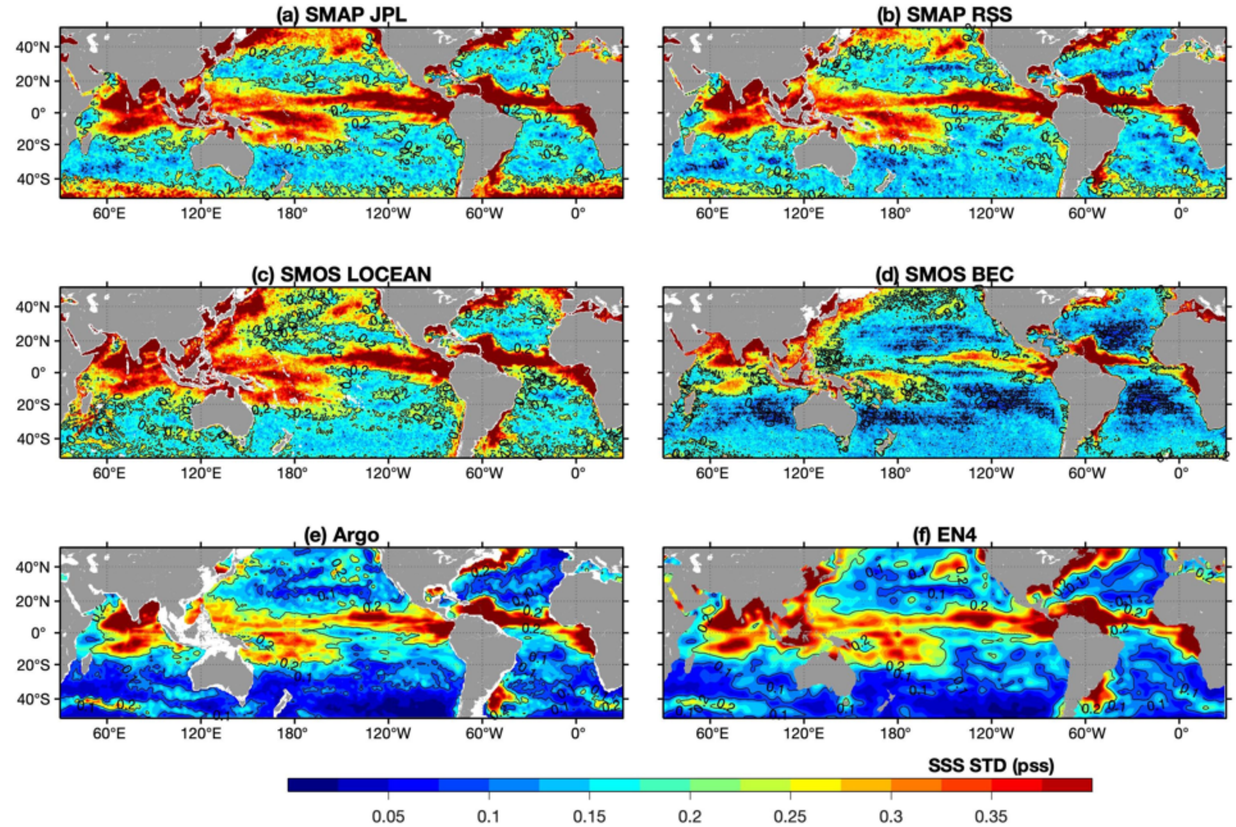

Figure 4. Standard deviation of monthly-mean SSS based on (a) SMAP JPL, (b) SMAP RSS, (c) SMOS LOCEAN, (d) SMOS BEC, (e) Argo, and (f) EN4.

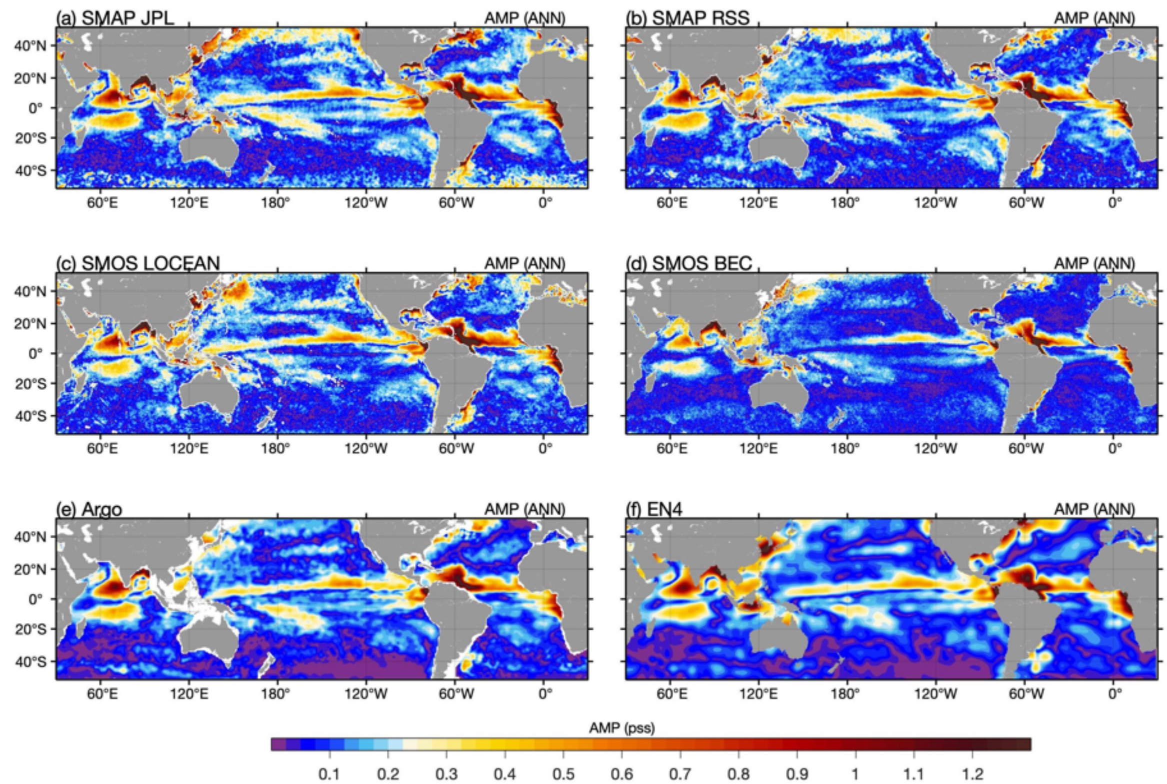

Figure 5. Amplitude of the estimated annual harmonic for (a) SMAP JPL, (b) SMAP RSS, (c) SMOS LOCEAN, (d) SMOS BEC, (e) Argo, and (f) EN4.

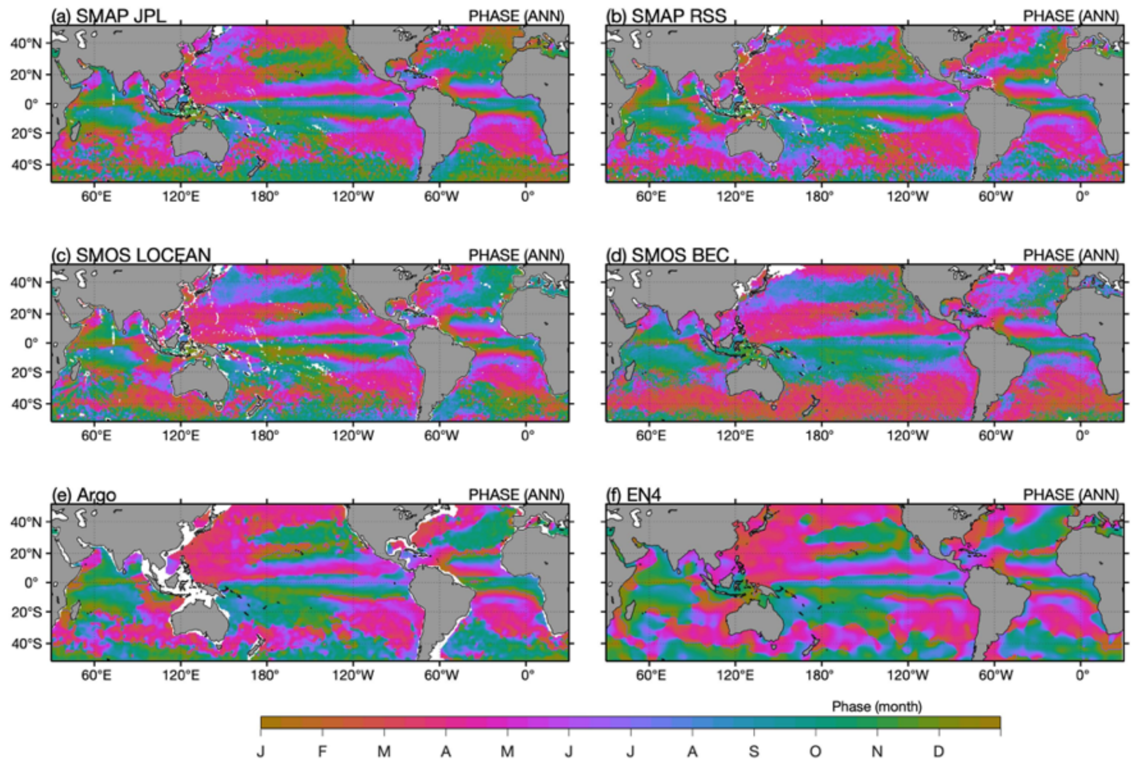

Figure 6. Phase of the estimated annual harmonic (i.e. month of the year of the maximum SSS) for (a) SMAP JPL, (b) SMAP RSS, (c) SMOS LOCEAN, (d) SMOS BEC, (e) Argo, and (f) EN4.

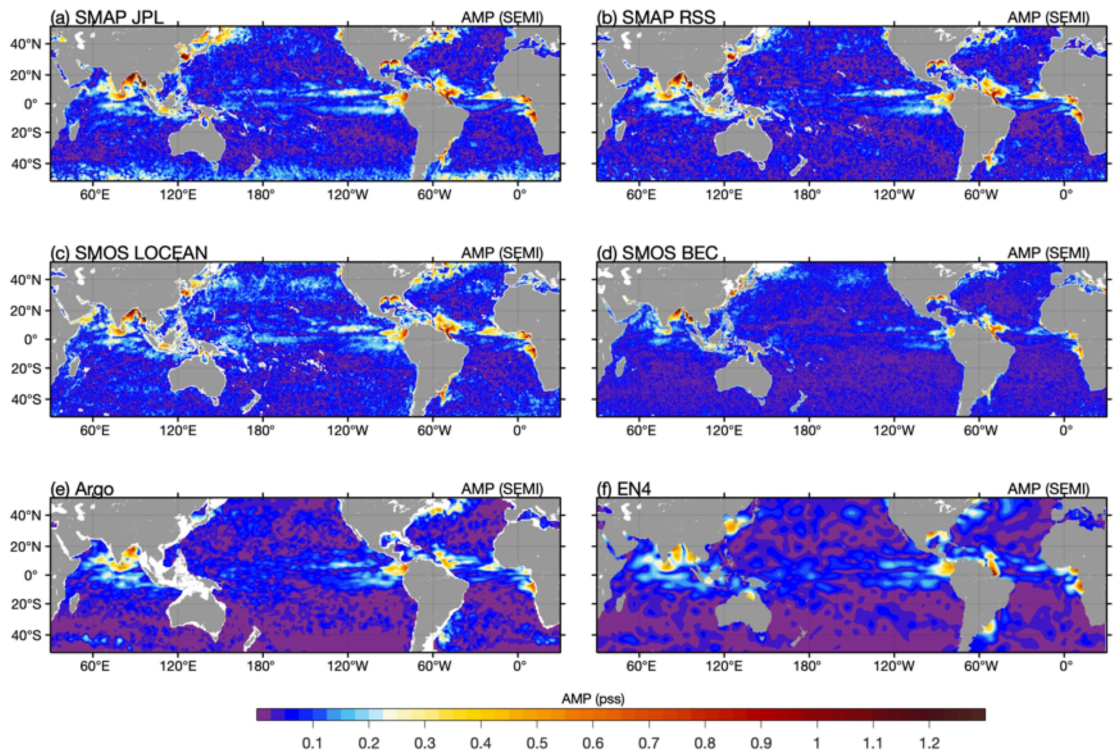

Figure 7. Same as Figure 5 but for the estimated semiannual harmonic

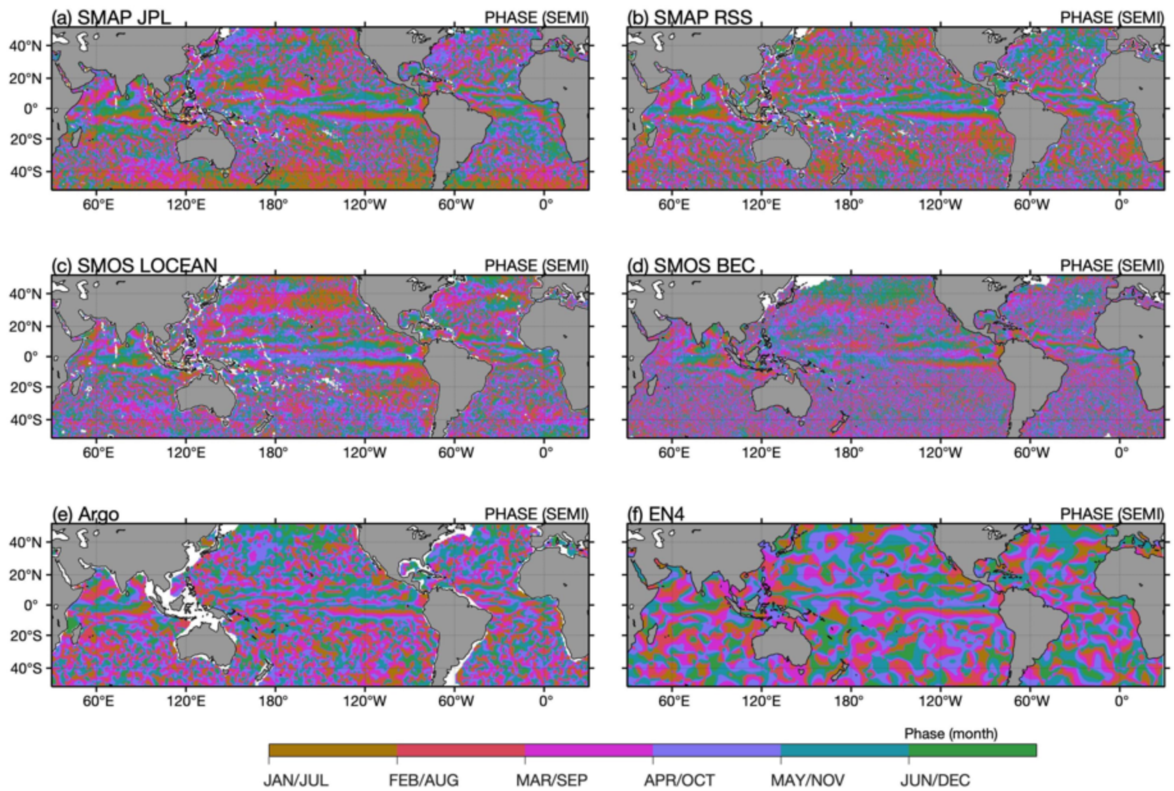

Figure 8. Same as Figure 6 but for the estimated semiannual harmonic. The cycle goes from January to June and repeats in July – December.

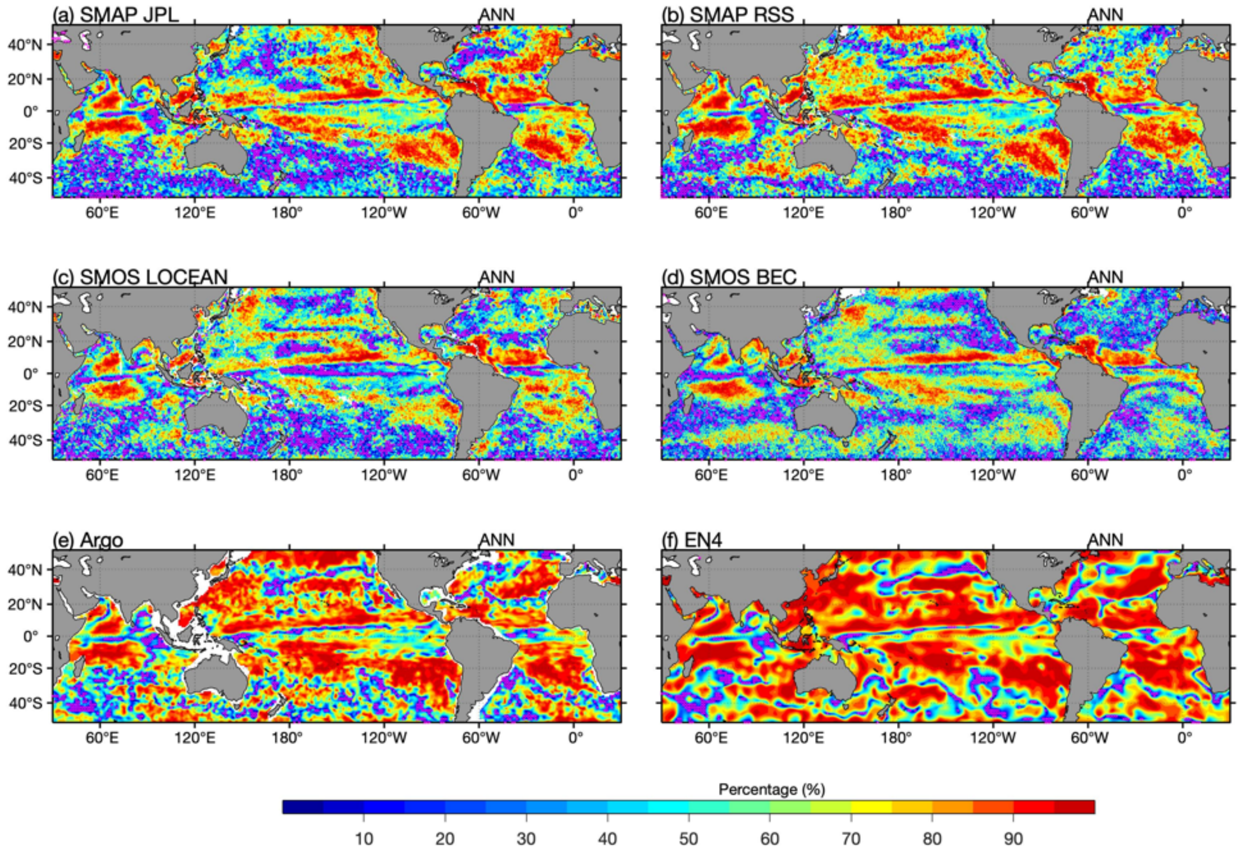

Figure 9. R^2 values (%) showing the percentage of the observed variance explained by the annual harmonic. The F-statistic values less than 0.95 were considered not statistically significant and shaded in magenta.

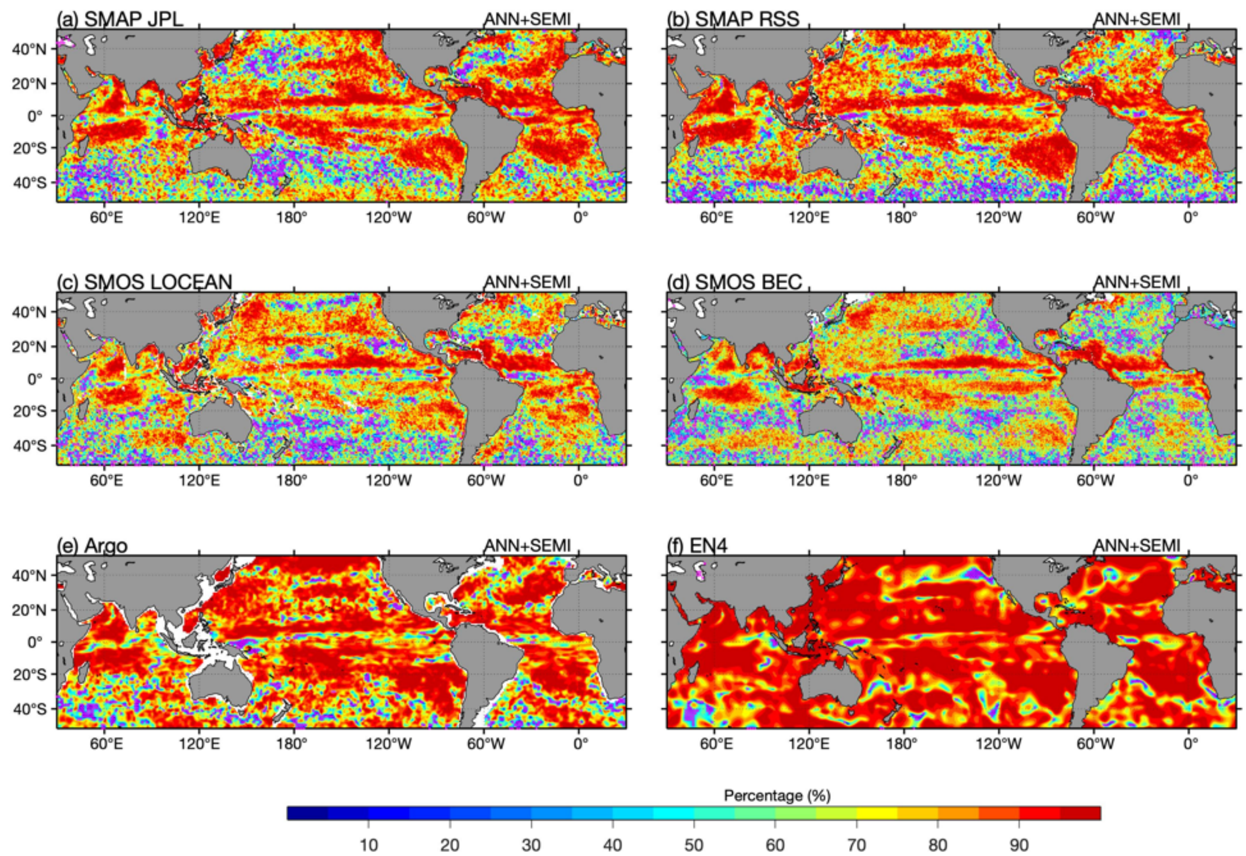

Figure 10. Same as Figure 9 but for the seasonal cycle reconstructed from annual and semiannual harmonics.

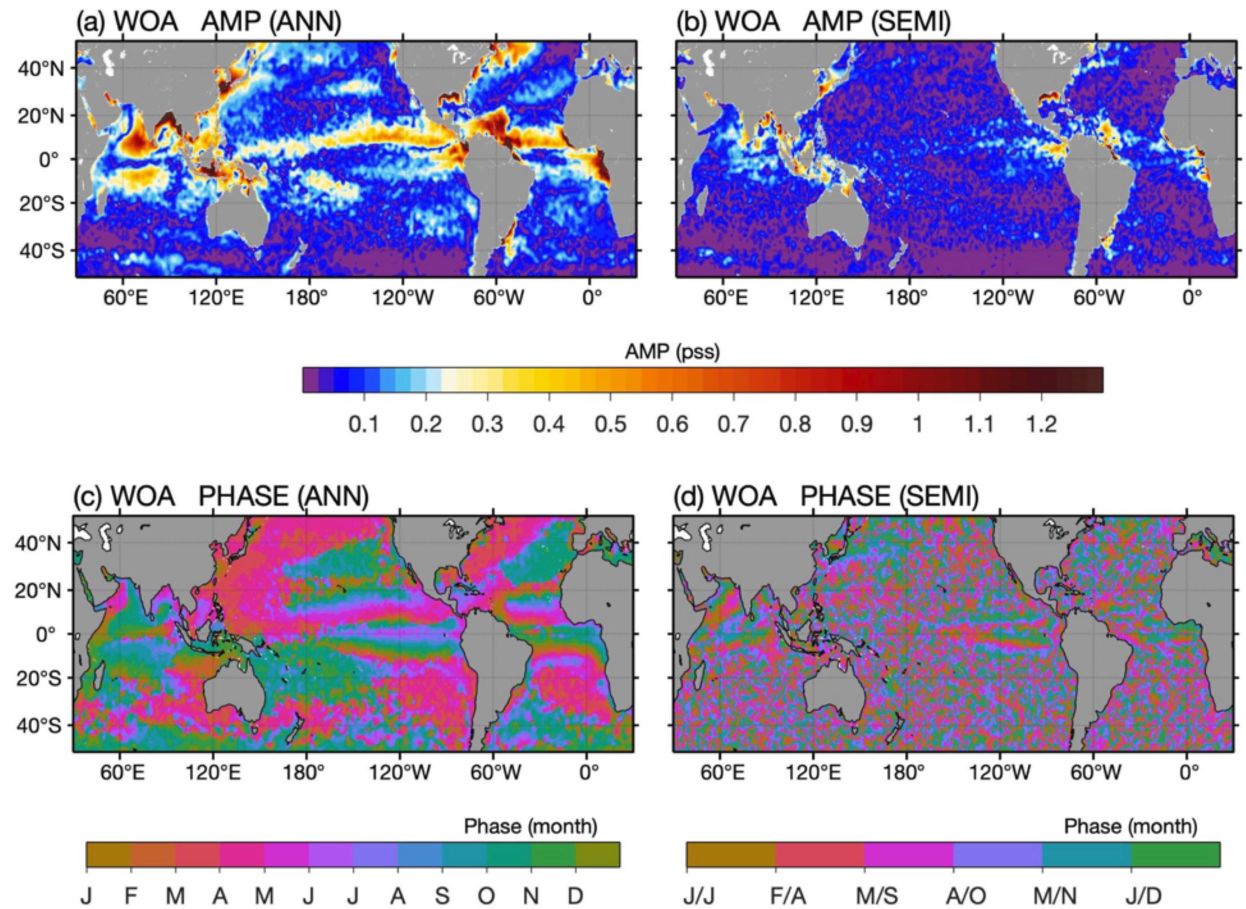

Figure 11. The first and second harmonic modes estimated from WOA. Amplitude of (a) annual and (b) semiannual harmonic, and phase of (c) annual and (d) semiannual harmonic (the cycle goes from January to June and repeats in July – December).

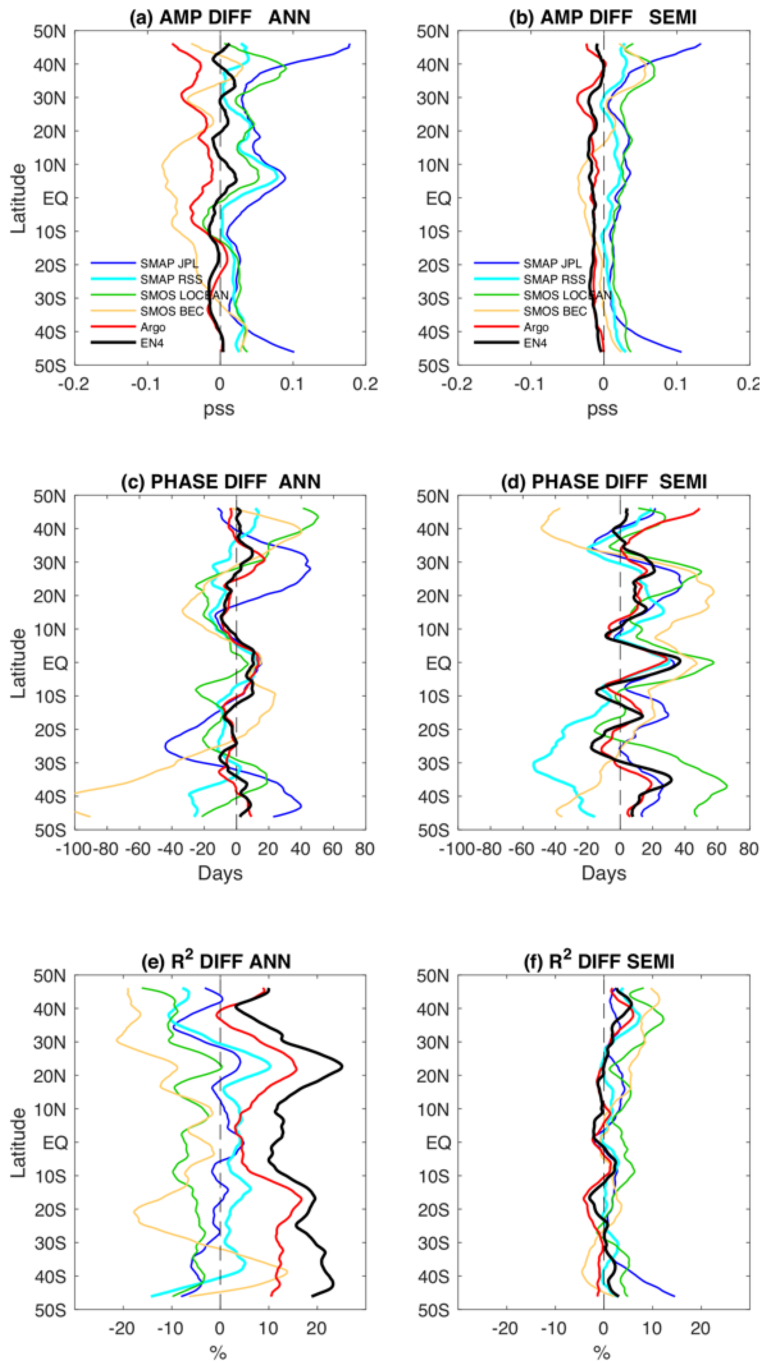

Figure 12. Zonally averaged differences between SSS products and WOA for the annual and semiannual parameters. Amplitude of (a) annual and (b) semiannual harmonic, phase of (c) annual and (d) semiannual harmonic, and R2 of (e) annual and (f) semiannual harmonic. A 15-point running mean along latitude was applied.

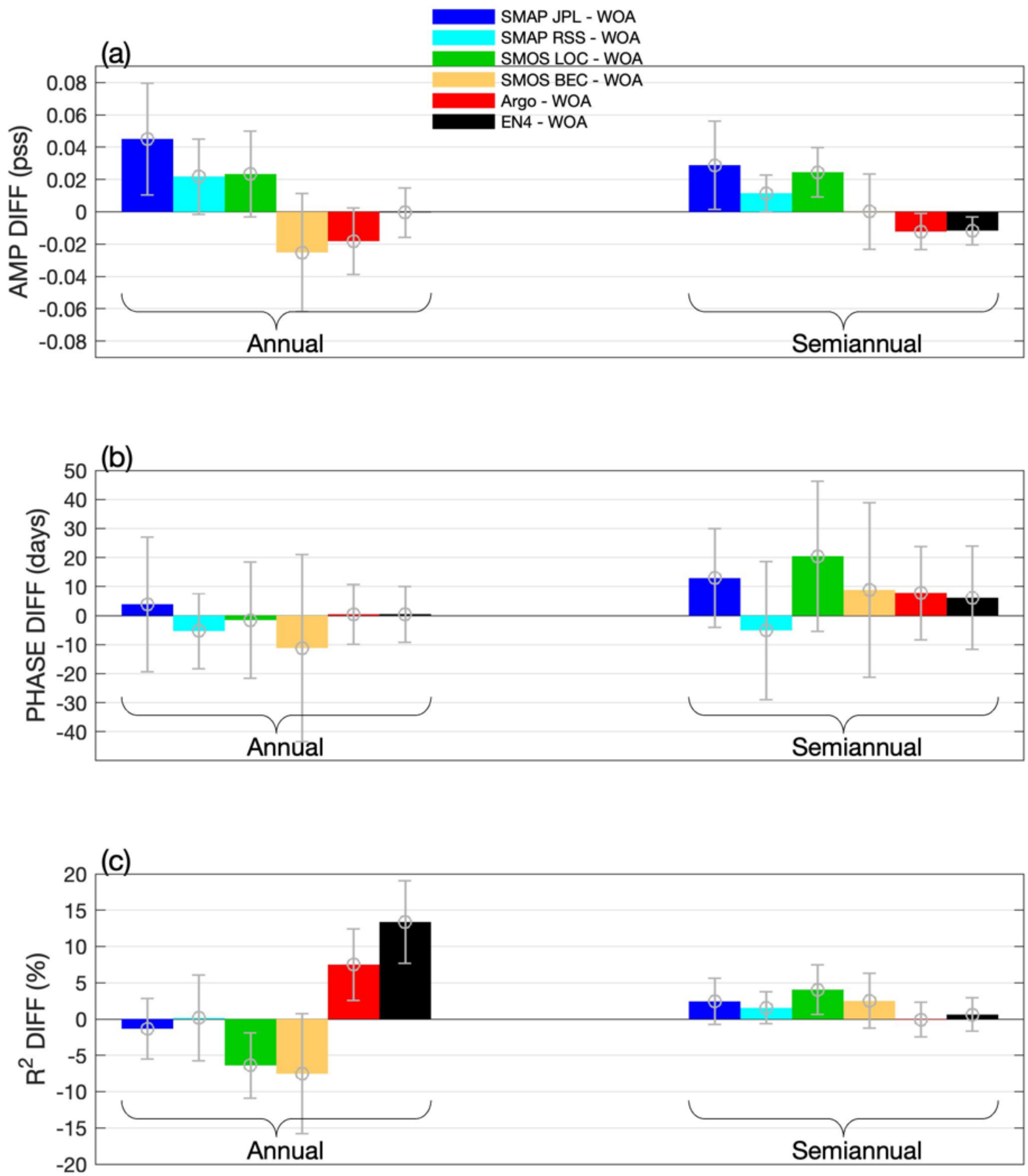

1253

1254 Figure 13. Global averages of the differences between SSS products and WOA in annual and

1255 semiannual parameters. (a) amplitude, (b) phase, and (c) R^2. Error bars represent one standard

1256 deviation from zonal mean at each latitude.

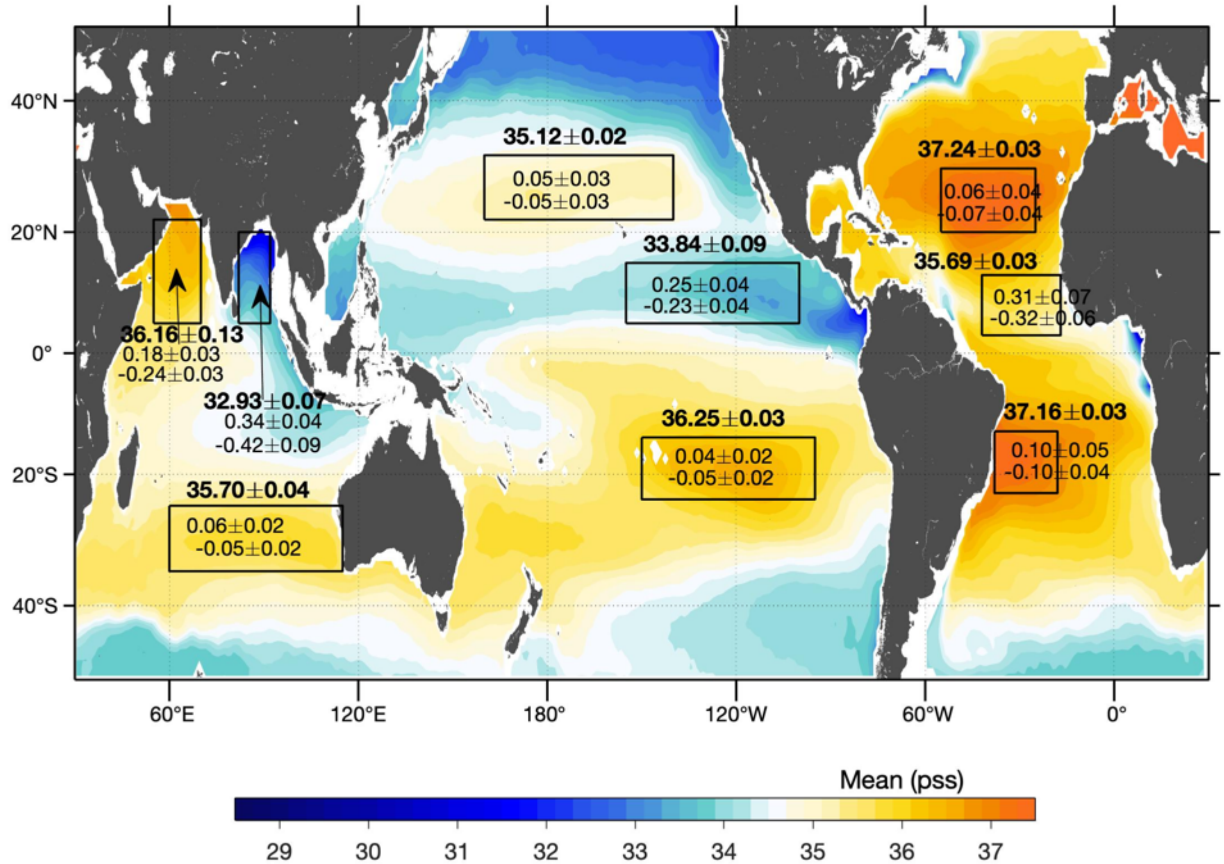

Figure 14. Summary of the mean, standard deviation (bold-face numbers), and the seasonal ranges (light-face numbers) for each boxed region. The mean and standard deviation were computed as the product ensemble mean and spread (STD) (see Table 2). The seasonal ranges were based on the maximum and minimum estimated from the reconstructed time series averaged over the nine selected boxes (see Table 4). Color shading shows the ensemble mean SSS of the six products over the period of 2016-2018 (same as Figure 3a).